Development of the 3pi CHICSi telescope

van Veldhuizen, E.J.

Award date:
1995

Development of the 3π
CHICSi telescope

E.J. van Veldhuizen

VDF/NK 95-14

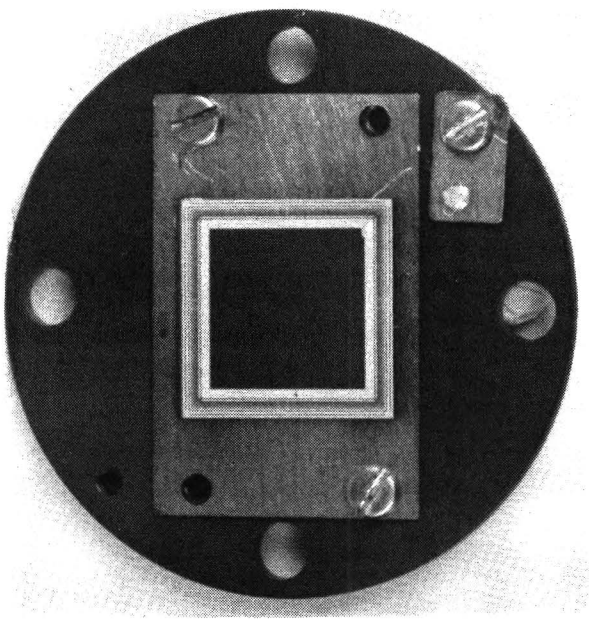

Foto: SINTEF silicon detector of 300 μm thickness and active area of 9.5 x 9.5 mm, mounted on a copper/teflon frame.

Graduation professor: M.J.A. de Voigt

Supervisor: L. Westerberg

With help of: V.V. Avdeichikov, H.J. Whitlow, M. el Bouanani and J. Romanski

Abstract

The CHIC collaboration performes research on heavy-ion collisions using the CELSIUS storage ring at the The Svedberg Laboratory in Uppsala. A design is made for making a 3π mass-analyzing telescope, called CHICSi, with around 1700 ΔE-E telescopes, each with an area of 1 cm^2. These telescopes will be made of silicon detectors with a thickness of 10, 300 and 500 μm. Also a GSO scintillator crystal with photo-diode readout will be used in some telescopes. For low energy (0.05 - 1 A MeV) fragments Time-of-Flight - Energy telescopes will be used.

The aim of my project was to test and improve these telescopes and to look at an alternative technique (Pulse Shape Analysis) to see whether it can be an alternative for ΔE-E telescopes.

To perform tests in a clean vacuum, a new chamber was designed and installed at a beamline from a tandem van de Graaff accelerator.

Measurements were done with silicon detectors fabricated by SINTEF. Configured in a ΔE-E telescope, they can deliver full mass separation for the measured ions up to silicon and energies up to 150 MeV. Unfortunately, these detectors were seriously radiation damaged at a very low (10^6 particles/cm^2) dose. Also channeling in the thin detectors was observed. This gives background events. With two available detectors placed in the reaction chamber in the CELSIUS ring, measurements were done to see the magnitude of the pick up of the high frequency electro-magnetic structure that is used in the ring. This signal was in the used detectors too small to give a serious disturbance of the signal. But a more important role is expected when the thin detectors will be used. Also STIM measurements were performed to obtain the thickness variations of the 10 μm detector. The local variations are below 0.2 μm, but the detector is 1.5 μm thicker at the edge than in the center. Also a start was made to look at the relation between the energy loss in the thin detector and the signal it gives.

The measurements done with a telescope that contained a GSO crystal with a photo-diode readout gave isotope separation for all (observed) ions up to carbon. The light output relation for a GSO crystal was determined. Monte Carlo simulations for the ion tracks in the crystal were checked and were in 20 % consistence.

The Pulse Shape Analysis (PSA) was performed with several detectors. With the present type of detectors, a mass separation for ions with a minimal energy of 2 A MeV can be obtained. This value is too high for use in CHICSi. A new type detector specially designed for PSA was tested for homogeneity in resistivity.

Simulations were performed to get more insight in a time-detector design that gives an observed time resolution of 80 ns. The simulation shows a resolution of 60 ns, and reveal the reasons for this good performance.

Contents

Chapter 1

Introduction

The The(odor) Svedberg Laboratory (TSL) in Uppsala has an accelerator- and storage ring called CELSIUS, which is fed by the Gustav Werner cyclotron. The cyclotron can produce typically 50 A MeV ions (185 MeV protons), which can be accelerated in the ring to 470 A MeV (1.36 GeV protons). The storage ring is mostly used for collisions between the accelerated ions and a gas target. The fragments of the reaction are detected and give information about the reaction dynamics. One of the groups that use the storage ring is the CHIC (CELSIUS Heavy Ion Collision) collaboration with participating institutes in Lund, Uppsala, Copenhagen, Gothenburg, Oslo, St. Petersburg, Bergen, Paris, Grenoble and Catania. This collaboration uses heavy ion collisions to find out whether substantial compression of nuclear matter can be achieved. Also it wishes to get insight in the nuclear equation of state far away from the ground state and multi fragmentation processes. A multi-fragmentation process occurs after two heavy ions have collided and form a nucleus far from the ground state with a high mass number. The nucleus is too heavy to return to the ground state without expelling a part of its mass. There are three mechanisms proposed for this process. At low energies, the particles leave the nucleus sequentially and a rather heavy remnant can survive. At higher energies, only one or two remnants are left. But when the system receives so much excitation energy that it is able to break into a number of fragments throughout its entire volume, it is called simultaneous break up. The fragmentation and the production of intermediate mass fragments (IMF) can be identified through multi-particle correlations. Therefore a project inside CHIC was started to build a mass-analyzing telescope that is able to cover almost the whole 4π angle around the reaction center. Since most detectors will be made from silicon, this project was called CHICSi ([GUT93]). The CHICSi telescope works with ΔE-E analyzing technique. The energy loss of a charged particle in a thin silicon detector is measured as well as the remaining energy. The mass of the particle can be derived from these energies. The telescope will consist of 16 rings with 32 ΔE-E telescopes each. Due to different expected energies at different angles, there will be three different kinds of ΔE-E telescopes used:

θ (degr.)	No. of rings	ΔE detector	E detector	veto detector	Energy range (A MeV)
15 - 40	6	10 μm Si + 300 μm Si	6 mm scintillator + photo diode	300 μm Si	0.7 - 60
40 - 90	6	10 μm Si	500 μm Si	300 μm Si	0.7 - 8.0
95 - 165	4	10 μm Si	300 μm Si	300 μm Si	0.7 - 7.0

This configuration covers 3π of the space. The most forward angles have to be covered by another detector system, that still has to be developed.

The table above shows that there will be 1728 detectors that have to be read out. It not only need a large volume to place the electronics, but it is also, from a vacuum point of view, almost impossible to have that many leadthroughs in an ultra high vacuum chamber. Therefore, a custom made chip is designed that will be put at every telescope. The chip will take care of the amplifying,

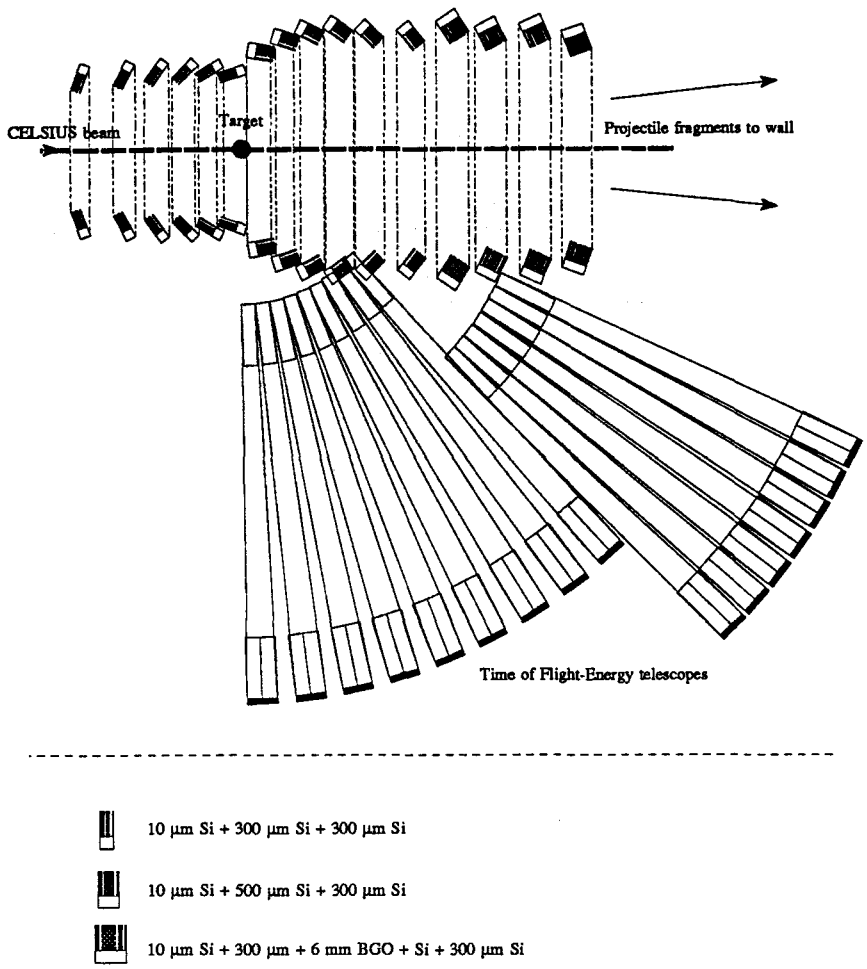

Figure 1.1: *Horizontal cross section of the CHICSi telescope.*

multiplexing of the readout and has a sophisticated trigger system that provides a number of signals that can be handled by conventional electronics, to allow triggers on IMF multiplicity, light particles, total multiplicity, spatial correlations etc. Due to the high capacitance of a thin detector, a normally designed pre-amplifier would not match this capacity and have a too high electronic noise level. Therefore, the on-chip pre-amplifier is specially designed, to decrease the noise.

Due to the thickness of the ΔE detector, particles with energy below 0.7 A MeV cannot be detected with the silicon telescopes. Therefore a concept is made to use Time of Flight-Energy (ToF-E) telescopes that can detect particles in the energy range from 0.05 A MeV to 0.7 A MeV. A schematic drawing of the CHICSi telescope and the ToF-E detectors is shown in figure 1.1.

The main subject of the final project for my study of Applied Physics at the Eindhoven University of Technology was the testing and improving of the telescopes, used for the CHICSi setup, at the The Svedberg Laboratory in Uppsala.

The silicon ΔE-E telescopes have thin detectors with a thickness of only 10 μm. Most detector producing companies are not familiar with the fabrication of this kind of detectors. To look at

the performance of the prototypes of these thin detectors and the thick detectors, many tests were performed. These are described in chapter 4.

As scintillator was chosen a cesium doped Gd_2SiO_5 (GSO) crystal ([AVD94]). Its ultra high vacuum compatibility, the high stopping and good timing properties makes this type ideal for the CHICSi telescope. Instead of the normally used photo-multiplier tubes, that are difficult to handle in ultra high vacuum, photo-diode readout will be used. Because not much research has been done with GSO crystals and especially in combination with photo diode readout, it needed some more detailed study. This will be described in chapter 5.

The decision of which components to use for the ToF-E telescope was already taken when I started my project. The design is discussed in appendix H. Since (for our needs) the time detector determines the mass resolution of the whole telescope, it is very useful to look at alternative time detectors. In one of the experiments at the TSL, a time detector developed in St. Peterburg is used for measurements of fission fragments. The claimed time resolution was a few times better than the expected resolution of the detectors that will be placed in the CHICSi telescope. Although the detector from St. Petersburg does not meet the requirements in size, it is very useful to *understand* why this design function that well. Therefore, I have performed computer simulations on this detector. This is described in chapter 7.

The individual telescopes in the CHICSi rings have to be able to determine the mass and the energy of the incoming particles. There are other methods than the ΔE-E technique to get this job done. During the project, very nice results became available ([PAU94]) about the use of pulse-shape analysis (PSA). The use of PSA will require less detectors for the CHICSi telescopes and would make the construction easier. But since PSA is never used to get full mass information, a substantial amount of further development has to be done to get this analysis technique useable. A little piece of that development is described in chapter 6.

Chapter 2

Theory

2.1 Ions in matter

2.1.1 Stopping power and range

Charged energetic ions lose their energy when travelling in matter mainly by interactions with the electrons in the matter. This is called electronic stopping. A small part of the stopping is due to interactions with the nuclei and is called nuclear stopping.

The electronic stopping was first described with classical mechanics by Bohr and later quantum-mechanically by Bloch. This resulted in the widely used Bethe-Bloch function ([KRA88]):

$$\frac{dE}{dx} = \frac{(}{e(2}4\pi\epsilon_0)^2 \frac{4\pi z^2 N_o Z\rho}{mc^2\beta^2 A}[\ln(\frac{2mc^2\beta^2}{I}) - \ln(1-\beta^2) - \beta^2] \tag{2.1}$$

The ion has in this equation a charge z, density of the matter is given with ρ and the mass and the charge of the atoms A and Z, m is the electron mass and β is given by $\beta = v/c$. The parameter I has to be adjusted for the kind of ion. This equation can give errors around several percent. Therefore it is more accurate to use measured data, that is fitted to a many parameter equation. An equation that is often used in computer programs and gives the range of the ion in matter is:

$$R = \frac{m}{z^2}(P_{(1,Z)}x^{P_{(2,Z)}} - P_{(3,Z)} - P_{(4,Z)}e^{P_{(5,Z)}x} - P_{(6,Z)}x^{P_{(7,Z)}x}) \tag{2.2}$$

with x given by

$$x = \frac{E}{m} \tag{2.3}$$

The energy, mass and charge of the ion is given by E, m and z. This equation has a different set of 7 parameters (P) for a the combination of (the atomic number of) the incoming ion and the kind of matter. These parameters for ions up till aluminium falling into silicon are given in appendix A. The energy loss in a thickness d and initial energy E can be obtained by finding an energy E' that fulfil:

$$R_{m,z}(E') = R_{m,z}(E) - d \tag{2.4}$$

The energy loss is then given by

$$E_{loss} = E - E' \tag{2.5}$$

Equation 2.2 has only different parameters for ions with different atomic number. For the different isotopes, it gives an approximation. It can be therefore sometimes be better to use a different equation, that has parameters for each isotope. It turns out that the following equation gives a good approximation ($< 0.1\%$) on an energy interval of 4 orders of magnitude:

$$R(E) = \exp\{p_1 + p_2\ln(E) + p_3\ln^2(E)\} \tag{2.6}$$

Also, the energy loss can be obtained in an analytical way (saves time for computer systems) by equation 2.5, with E' given by:

$$E' = \exp\{\frac{-p_1 + \sqrt{p_1^2 - 4p_2(p_0 - \ln(R(E) - d))}}{2p_0}\} \tag{2.7}$$

It is obvious that this equation is only valid for a positive number below the square root sign. The parameters for several ions on an interval between 50 keV and 200 MeV are given in appendix B.

2.1.2 Nuclear reactions and kinematics

In the previous section, the interactions between ions and electrons were described. In this section the interactions between ions and the nuclei in matter are described. An ion can be scattered on a nucleus or undergo a nuclear reaction. Also, the nucleus itself can be kicked out and is then called a recoil.

Scattering

The scattering process of an ion on a nucleus can be described with classical mechanics. After an ion, with initial energy E_0 and mass m_1, is scattered on a nucleus with mass m_2, it has a remaining energy E_1 The ratio between the the remaining and initial energy depend on the scattering angle θ and is given by ([BRA91]):

$$K = \frac{E_1}{E_0} = [\frac{x\cos\theta + \sqrt{1 - x^2\sin^2\theta}}{1+x}]^2 \tag{2.8}$$

with

$$x = \frac{m_1}{m_2} \tag{2.9}$$

For $m_2 < m1$ ($x < 1$) and for angles up till $\theta_{max} = \arcsin(\frac{1}{x})$, there is a second solution for the kinematic factor:

$$K = \frac{E_1}{E_0} = [\frac{x\cos\theta - \sqrt{1 - x^2\sin^2\theta}}{1+x}]^2 \tag{2.10}$$

Recoils

For the recoils, the kinematic factor, with E_2 the energy of the recoil and ϕ the angle, is given by

$$K_{recoils} = \frac{E_2}{E_0} = 4\frac{m_1 m_2}{(m_1+m_2)^2}\cos^2\phi \tag{2.11}$$

Nuclear reactions

There are two important parameters that determine whether a nuclear reaction can occur. These are the Coulomb barrier and the reaction Q-value.

An ion has to overcome the electric repulsion from a nucleus, to come close enough to the nucleus to be able make a nuclear reaction. The minimum energy required to overcome this Coulomb barrier is given by

$$E_{CB} = \frac{1.44 Z_1 Z_2 (1 + \frac{M_1}{M_2})}{1.25(M_1^{\frac{1}{3}} + M_2^{\frac{1}{3}})} \tag{2.12}$$

with Z_1 and Z_2 the atomic numbers of the two nuclei and a_0 the Bohr radius and E given in MeV.

The Q-value is the difference in total energy before and after a nuclear reaction. A positive Q-value

for a nuclear reaction implies that when the two nuclei can come close enough, the reaction can occur. For negative Q-values, there is a minimum required (kinetic) energy ($T_{threshold}$), for which the reaction can occur. For a reaction X(a,b)Y and m_i the mass of particle i, the threshold energy is given by:

$$T_{threshold} = \frac{m_Y + m_b}{m_Y + m_b - m_a} \tag{2.13}$$

2.1.3 Channeling

By describing most physical properties of interactions between ions and matter (like scattering and stopping), it is assumed that the ion has a random probability of interacting with atoms and electrons. There is however a phenomenon that is called 'channeling' ([MOR73]). In that case, an ion travels through a channel that exists by the regularity in the crystal. Channeled ions cannot get close enough to the atomic nuclei to undergo large angle Rutherford scattering. Also the probability of interacting with electrons is different for non-channeling ions. This gives that channeled ions undergo different stopping ([DIJ94]).
A channeling ion can be forced to leave its channel. This is called dechanneling. This is not only due to imperfections in the crystal, but also physical phenomena ([MOR73]). There is a maximum critical angle Ψ_c, for which an incoming ion can channel.

$$\Psi_c^2(\rho) = \frac{2(2\pi)^{\frac{1}{2}} Z_1 Z_2 a_0 E_R}{Ed} \frac{\exp\{-m(1 + x_{rms}^2/a^2)^{\frac{1}{2}}\}}{(1 + x_{rms}^2/a^2)^{\frac{1}{2}}} \tag{2.14}$$

In this equation, Z_1 and Z_2 are the atomic numbers of the ion and the target (the matter the ion has to channel in), E is the energy of the ion, E_R the Rydberg energy (13.6 eV) and d is the atomic spacing. A practical value for the mean square thermal vibrational amplitude x_{rms}^2 is given in [BRA91] as 0.1 Å. The value for m should be between 1 and 3. The Thomas-Fermi screening distance a is given, with a_0 the Bohr radius, by

$$a = \frac{a_0}{(Z_1^{\frac{3}{2}} + Z_2^{\frac{3}{2}})^{\frac{1}{2}}} \tag{2.15}$$

Not all ions with an angle less than the critical angle will channel. It will depend on where the ion impinge with respect to the atom strings. Although, for perpendicular incoming ions to the sample, the fraction channeled ions can be up to 99 % ([BRA91]).

2.2 Silicon detectors

The semiconductor silicon has a small energy gap between the valence band and the conduction band. When an electron makes a transition from the valence band to the conduction band, an electron hole pair is created. This creation of pairs is constantly done by the thermal energy, but an equilibrium exists due to recombinations. Also charged particles will create electron-hole pairs inside the detector. This will give a current proportional to the number of electron-hole pairs produced. This is the basic principle for the silicon detector. To enhance its qualities, one has to modify the material.

In pure silicon, the number of holes equals the number of electrons in the conduction band. This balance can be changed by introducing a small amount of impurity (dope) atoms having one more or less valence electrons in there outer atomic shell. This create n-type (for pentavalent doping) or p-type (trivalent doping) semiconductors.

Most silicon charged-particle detectors are made from n-type silicon, created by irradiating pure silicon with neutrons ($^{28}\mathrm{Si} + \mathrm{n} \rightarrow {}^{29}\mathrm{Si} \rightarrow {}^{29}\mathrm{P} + \beta^-$). A p-n junction is created by shallow diffusion of p-type material at the surface. At the p-n junction, a range of immobile space charge is created

and is called the depletion zone. The width of the depletion zone d depends on the resistivity ρ and the internal voltage V by:

$$d = c\sqrt{\rho V} \tag{2.16}$$

The parameter c depends on the semiconductor. For n-type silicon, the value is 0.53. For ρ given in Ωcm and V in volts, d is then given in μm. To enlarge the depletion depth (and therefore the active volume of the detector) and enhance the charge collection, a reverse bias voltage is applied during operation of the detector. This also will induce a certain current flow, called the leakage current.

The signal of the detector is proportional to the created electron-hole pair. Since on the average for every 3.62 eV energy loss of the ion, one electron-hole pair is created, the signal (total charge from the detector) is also proportional to the energy loss of the ion in the detector. An exception is described in next section.

2.2.1 Pulse Height Defect

It is a well known fact ([WIL70], [STE71] and [KAU73]) that the response of a silicon detector differ for different kind of ions with the same energy. Since heavier ions give a slightly lower pulse compared to lighter ions, this effect is called 'the pulse height defect' (PHD). According to [CLI90], the PHD is caused by three effects.

- The entrance window defect. The energy loss of ions in the dead layer of a detector strongly depends on the kind of ion.
- The nuclear stopping defect. The nuclear stopping and the electrical stopping (the latter is creating the signal) are two independent functions of energy and differ for every kind of ion.
- The residual effects that arises from various contributions, such as plasma recombinations, trapping and carrier diffusion, that ultimately produce an incomplete charge collection.

There are several semi-empirical equations to describe the PHD. I will describe the one that gave the most reliable results in [LOV95].

The PHD $\Delta\epsilon$ for an ion with real energy ϵ in LSS units is given by

$$\Delta\epsilon(\epsilon) = \frac{6\epsilon}{\epsilon + 8} + \frac{A}{1 + 525\epsilon^{-1.407}} \tag{2.17}$$

The parameter A depends on the detector and mainly on its resistivity. For low resistivity detectors (around 1 kΩ cm), A has the value around 20. The conversion from SI units to the dimension less LSS units can be done by:

$$\epsilon = E\frac{0.8853a_0(Z_1^{\frac{3}{2}} + Z_2^{\frac{3}{2}})^{-\frac{1}{2}}M_2}{Z_1 Z_2 e^2(M_1 + M_2)} \tag{2.18}$$

2.2.2 Pulse Shape

When an ion passes a silicon detector, it creates electron-hole pairs. The electrons drift to the positive side of the detector and the holes towards the negative. This charge collection directly forms the shape of the current pulse that comes from the detector. Two ions with the same energy, but with different masses gives different pulse shapes. This can be explained by two processes ([PAU95]).

The first process that makes the pulse shape dependent on the ion mass is the difference in stopping between ions with different masses. This means that two different ions with the same energy will create electron-hole pairs with a different depth-ionisation distribution in the detector. The drift

velocity for the electrons (v_-) and holes (v_+) depends on the internal electric field F and the intrinsic mobility $\mu_{+,-}$.

$$v_\pm \approx \mu_\pm F \tag{2.19}$$

Normally μ_- is 2 or 3 times higher is than μ_+. Therefore the slow holes will dominate the pulse shape. Also, the field F is linear with respect to the depth in the detector ([AVD95]). Only when the detector is operated in reversed geometry (particles impinge at the ground side of the detector), the holes will have a longer drift time for heavier ions in a n-type detector.

The second process that determines the mass dependency of the pulse shape is the plasma erosion effect, that plays an important role especially for heavier ions. When an ion passes a silicon detector, it creates a plasma. Since the plasma acts as a conductor, there cannot be an electric field inside this plasma. The decay of this plasma column happens by diffusion and removal of the charge carriers, with a typical decay time τ_{pl}

$$\tau_{pl} \sim \frac{\sqrt{\Delta Q/\Delta x}}{F} \sim \frac{\sqrt{|dE/dx|}}{F} \tag{2.20}$$

Wherein $\Delta Q/\Delta x$ is the charge per depth interval, and this charge is created by the electrical stopping dE/dx. Since the stopping is higher for heavier ions, it is clear that the plasma erosion makes the charge collection for these ions slower and therefore decreases the risetime of the pulse.

2.2.3 ΔE-E telescope

A ΔE-E telescope can be used to determine the mass and the energy of an incoming ion. Such a telescope consists of two detectors, mounted after each other. The first detector is used to detect the energy loss in the detector itself. The second detector gives information about the remaining energy. The energy loss in the thin detector can be calculated with the Bethe-Block equation (equation 2.1), and is in a simple form:

$$\frac{dE}{dx} = C_1 \frac{mz^2}{E} \ln[C_2 \frac{E}{m}] \tag{2.21}$$

with C_1 and C_2 two constants. Since the logarithm only varies slowly with the energy, and E is known by adding the energy of the detectors, one can determine mz^2, which gives the mass.

2.3 Scintillators

A scintillator crystal can convert the energy of an incoming energetic charged particle into light energy. The ion forces electrons in the crystal (which is normally an insulator) to make a transition from the ground state (valence) band to a higher (conduction) band, and thereby creating an electron-hole pair (or an exciton). The transition back to the ground state creates a photon that can be detected. But in reality, crystals have imperfection that disturb the bandstructure. In [BIR64], three causes for centers in the forbidden band are given:

- Luminescence centers, in which the transition to the ground state is accompanied by photon emission.
- Quenching centers, in which radiationless thermal dissipation of excitation energy may occur.
- Traps, which have metastable energy levels from which the electrons (or excitons) may subsequently return to the conduction band by acquiring thermal energy from the lattice vibrations, or fall to the valence band by a radiationless transition.

The luminescence and quenching centers arise from impurities, interstitial ions and/or defects, and they introduce local discrete energy levels.

In a perfect crystal and with a low ionization (so that the excitations cannot interact with each other), the 'specific fluorescence' (the light energy created per length interval) dL/dr is given by

$$\frac{dL}{dr} = S\frac{dE}{dr} \tag{2.22}$$

with S the absolute scintillation efficiency and dE/dR the specific energy loss.

For higher ionization densities BdE/dr (with B a constant) in imperfect crystals with quenching parameter k, Birks ([BIR64]) proposed the following semi-empirical formula:

$$\frac{dL}{dr} = \frac{S\,dE/dr}{1 + kB\,dE/dR} \tag{2.23}$$

For ions with energies above a few MeV per nucleon, one can use the approximation

$$\frac{dE}{dr} \simeq \frac{cAZ^2}{E} \tag{2.24}$$

with c a constant. Analytic integration delivers the light output over the range of the ion:

$$L(E) = a_0 + a_1\{E - a_2AZ^2 \ln|\frac{E + a_2AZ^2}{a_2AZ^2}|\} \tag{2.25}$$

In this equation, a_1 is the absolute scintillation efficiency S and

$$a_2 = ckB \tag{2.26}$$

With the boundary condition $L(0) = 0$, a_0 is supposed to disappear. But in experiments in covers the offset in the electronics.

Chapter 3

Experimental setup

To perform an experiment for testing a detector, you need a facility for holding the detector, electronics to amplify and filter the signals and a data acquisition system to store and analyze the data. These 3 facets are described in the next sections.

3.1 Chambers

As mentioned in the introduction, the aim of the project is to test some new designed detectors. This can be done with a radio-active source or by using an ion beam from an accelerator. In all cases, the tests have to be done in vacuum (< 1 Pa) to (in case of a source) prevent straggling in air and to operate the detectors on their full bias voltages. Therefore you need at least a vacuum chamber.

To test the energy resolution of a particle detector, a radio-active charged-particle source is sufficient for this purpose. The chamber used for this analyzing is described in section 3.1.1.

For testing the mass resolution of a mass analyzing telescope and see how it behaves under tough conditions, you need an ion beam that can produce (by nuclear reactions or scattering and recoils) particles with different masses and energies. For this purpose we used 3 different chambers. The choice which one to use depends on the requirements for the experiment.

For ions up till 3 A MeV, the Tandem van de Graaff accelerator is the cheapest alternative. Also, every 6 weeks a schedule is made, so it is easy to get beam time. A new chamber had to be designed. This is described in section 3.1.2. The Gustav Werner cyclotron can deliver ions around 50 A MeV. Since the cyclotron is also needed for the CELSIUS storage ring, it is not easy to get beam time. In section 3.1.3 is written more about the chamber for these experiments. It has not been possible during the time of this project to get beam time in the CELSIUS ring for detector development. It is however possible to perform so called parasitic measurements. In that case one can install detectors in the reaction chamber and measure at the same time as another experiment is performed. You do not have any influence on the kind of ion and its energy. Chapter 3.1.4 gives more details about this subject. For microbeam measurements, there is a facility in Lund available, which has pelletron accelerator. This beam line is described in 3.1.5.

3.1.1 Source scan

To test a detector with an alpha-source, there is a small test chamber available. The layout of this chamber is shown in figure 3.1. The basic setup is that the detector is placed in its holder and the source is placed at the other side of the chamber. The signals can be taken out by the BNC connectors. The quick flanges are connected to a pump system and a pressure gauge.

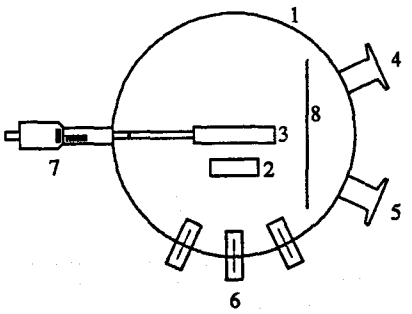

Figure 3.1: *Detector test chamber. 1) chamber 2) detector holder 3) collimator 4,5) flanges 6) BNC connectors 7) micrometer screw 8) plate to prevent a direct air flow*

A very nice feature of this chamber is that the holder for the collimator can be moved from the outside with a micrometer screw. Therefore it is possible to perform a line scan on the detector with a spot of 0.8 mm diameter. During all my experiments, the pumping system of the gamma cave chamber (see 3.1.3) was used and the reached pressure was around 10^{-4} mbar.

A ^{226}Ra source that gives alpha particles with several well defined energies (4.781, 5.305, 5.486, 6.000 and 7.688 MeV) and almost equal intensities (since the α's are produced in a decay string), is used to measure the energy resolution.

3.1.2 Tandem

The Tandem lab has a tandem van de Graaff accelerator that can produce ions till around 5 A MeV. The final energy depends on the charge state Q of the ions by $(Q+1)\cdot V_{terminal}$. A schematic view of the beam line is given in figure 3.2.

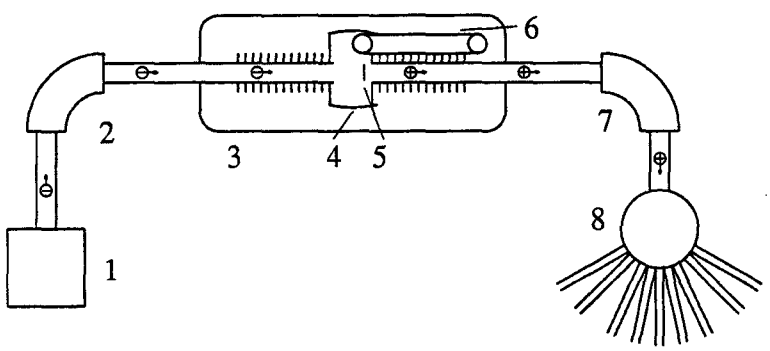

Figure 3.2: *schematic view of the tandem lab. 1) ion source 2,7) analyzing magnets 3) pressure tank 4) high voltage terminal 5) stripper tube 6) van de Graaff band generator 8) switching magnet*

Negative ions are produced in one of the three ion sources. They are accelerated to 150 keV. The first analyzing magnet makes sure that only ions with the proper charge to mass ratio are sent into the accelerator. The accelerator itself consists of a tank that contains pressurized gas. A van de Graaff generator delivers a high voltage (up to 5.5 MV) at the high voltage terminal. The negatively charged ions are accelerated towards the terminal. A stripper foil in the terminal strips most electrons away from the ions. This result in positively charged ions with a certain distribution amongst the different charge states. These ions are then again accelerated. An analyzing magnet bends only the ions with the right charge to mass ratio to the experiment hall. A switching magnet

delivers the beam to one of the 9 beamlines.

The old chamber that was used for testing detectors at the Tandem lab did not function well for our purpose. Therefore, I had to design a new one. It had to be mounted onto an experiment that already exists at the -25 degree beam line of the Tandem lab and is used for radiating thyristors and to do research on polymers.

The requirements for the chamber was that it should give a clean vacuum ([VAR84]), so that the detectors were not polluted when they have to be placed in the CELSIUS ring with a pressure of 10^{-8} Pa. It is not possible to test a detector by directly radiating it by the ion beam. This would destroy the detector immediately. Therefore the beam has to hit a certain target first. Due to several processes in the target a variety of particles are released. These particles can be used to test the detector.

To make the chamber fast in TSL's workshop, the concept was to use standard Conflat © flanges. This makes it possible to bake this chamber at a later stage of this project. In figure 3.3, the final design is drawn. Figure 3.4 gives a side view.

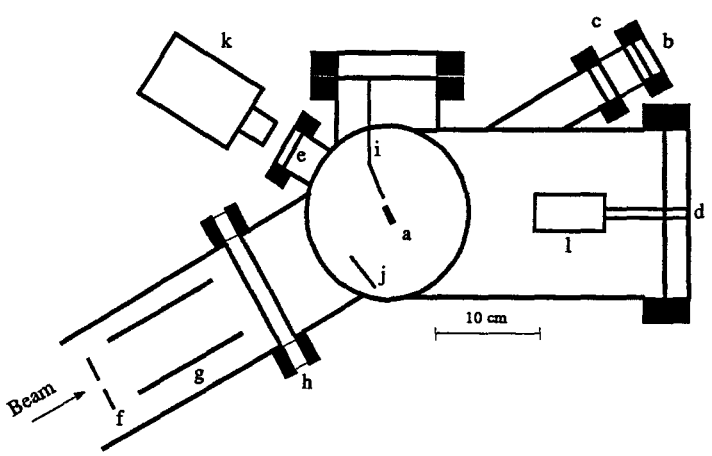

Figure 3.3: *Top view of the tandem detector test chamber. a) target b) Faraday cup c) ceramic break d) flange with electrical feedthroughs and possibilities to mount detectors e) view port f) collimator g) cryo trap h) nylon insulator ring i) screen j) shielding k) TV-camera* l) detector holder

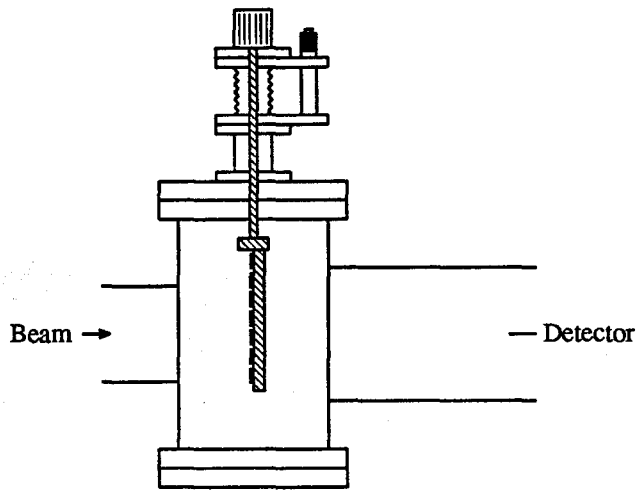

Figure 3.4: *Side view of the chamber.*

The beam hits the target and stops in the Faraday cup. This faraday cup consists of a tantalum plate that is mounted on a flange. This flange is isolated from the chamber with a ceramic piece, to provide the readout of the beam current. Detectors can be placed inside the chamber at angles between 15 and 45 degrees. To prevent ground loops and influences from the accelerator, the whole chamber is electrically isolated from the accelerator by a nylon ring. At a distance of 20 cm towards the accelerator, a tantalum collimator is placed with a diameter of 4 mm. For vacuum reasons, the collimator can not block the entire beam tube. Therefore shieldings are placed inside the chamber to prevent that the detector is hit during beam alignment and focusing or by scattering on the collimator. One of the shields is actually a screen. This screen can be monitored with a TV- camera for focusing purposes. One of the targets is made from ceramic screen material and is also used for beam allignement. Also a copper cold trap is placed in this section to prevent oil and other vapours from entering the chamber. For the vacuum there is a roughpump, a turbo-molecular pump and a cryo pump.

3.1.3 Gamma cave

The chamber in the gamma cave consists of a reaction chamber in the form of a standing cylinder with a diameter of 53 cm and a height of 30 cm. The chamber is placed in a beam line with the faraday cup placed in the end of the beam line, a few meters after the chamber.

The detectors can be placed on a platform that can be rotated around the target. This platform is electrically isolated from the chamber. Also the electrical feedthroughs are placed on an isolated flange. This makes it possible to use one common ground for all the electronics.

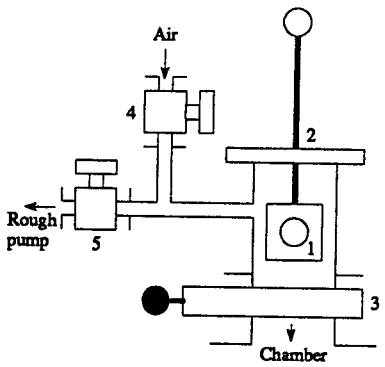

Figure 3.5: *target holder for the gamma cave chamber. 1) target 2) feedthrough 3,4,5) valves*

One target-foil at a time can be placed on a target holder that is connected to a rotational and linear motion feedthrough. This is shown in figure 3.5. The target can be changed without pressurizing the whole chamber. The target can be lifted and the target holder can be closed by a valve. By removing the whole target holder, the target can be changed.

3.1.4 CELSIUS ring

The CELSIUS ring is built to store and accelerate light (1.36 GeV protons) and heavy ions (470 A MeV for ions with charge-mass ratio of 0.5). Its circumference is 81.8 m. A layout of the ring is given in figure 3.6. A total layout of the cyclotron, the CELSIUS ring and all experimental areas are given in figure 3.7.

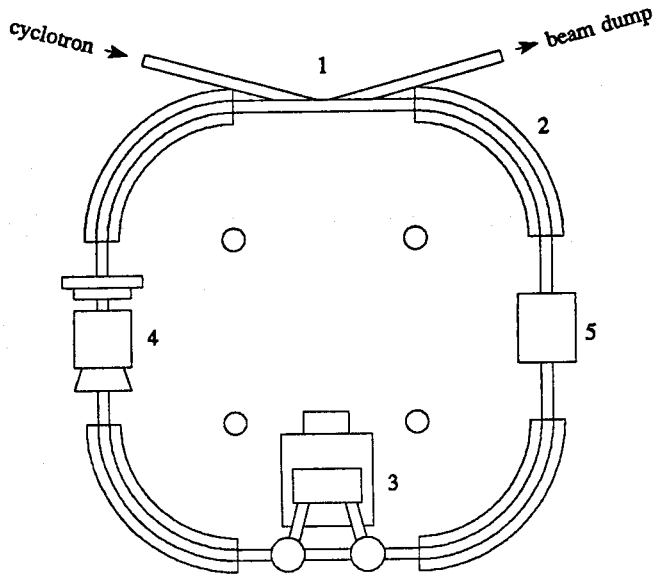

Figure 3.6: *Layout of the CELSIUS ring. 1) injection section 2) bending magnets 3) electron cooler 4) cluster-jet target 5) pellet target*

The beam is injected and extracted at the injection section. To get a lower energy spread of the particles in the beam, an electron cooler is placed at the other side of the ring. The other two straight sections are used for experiments.

The CHICSi telescope will be placed at the cluster-jet target. The chamber has to be modified to fit the CHICSi telescope. In the present chamber there is a flange at 135 degrees. There are two Intertechnique passivated ion implanted 300 μm detectors placed in this position. The detectors form a ΔE-E telescope.

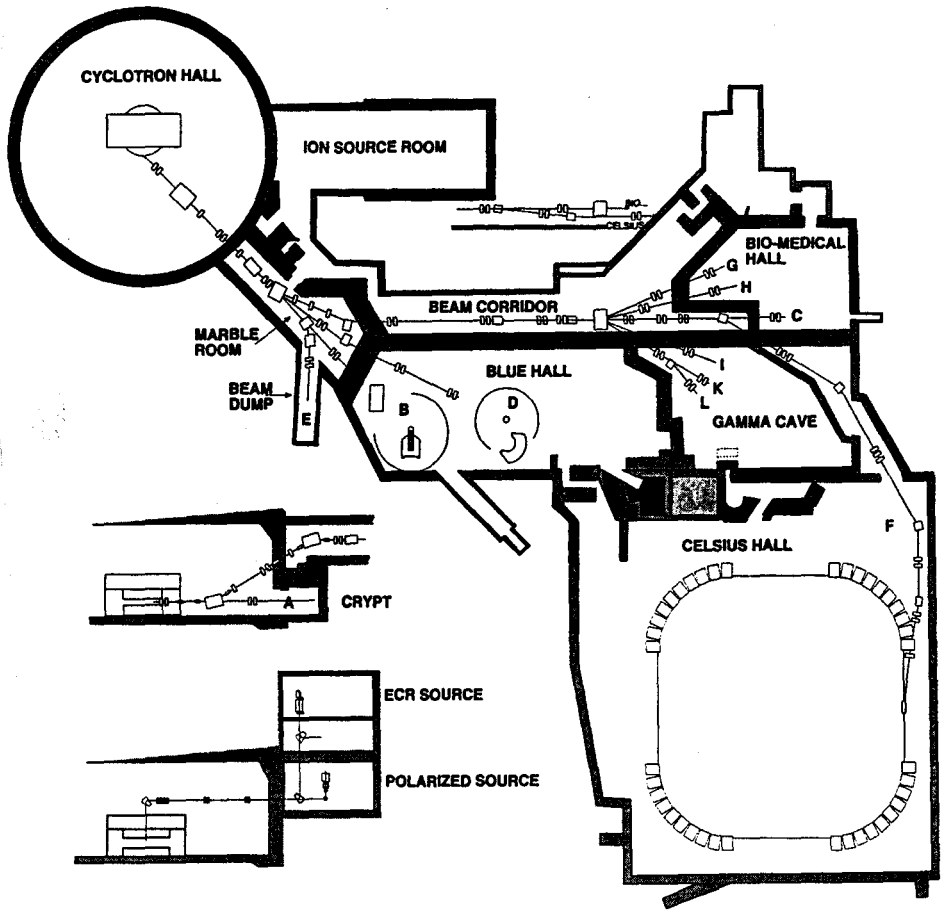

Figure 3.7: *Layout of the cyclotron, CELSIUS ring and experimental areas.*

3.1.5 Lund's microbeam facility

University of Lund has a micro-beam facility. A representation of this beam line is given in figure 3.8.

The accelerator is a pelletron accelerator that can give a proton beam between 0.9 and 3.2 MeV. The beam is focussed and bent by a switching magnet. It has to pass three slits. The last two slits are used as object and aperture slits to obtain the micro beam. Before the beam enters the chamber it is focussed by a triplet of quadrupoles. The beam can be moved around on the sample by a pair of scanning magnets. The beam line is kept under vacuum by three 700 l/s diffusion pumps. To make pumping down easier, pressurizing is done by injecting nitrogen gas into the beam line or chamber. The chamber itself contains mainly a target wheel that can contain 12 targets. The whole wheel can be remotely positioned in all the three dimensions by stepping motors. An X-ray detector is placed in the backward direction for PIXE (Particle Induced X-ray Emission) measurements. A moveable holder behind the target holds a faraday cup, the detector and the objective for the (optical) microscope.

Instead of using expensive particle detectors that would be damaged rather soon by the high particle dose, cheap Hamamatsu S1223-01 photo diodes are used for the STIM (Scanning Transmission Ion Microscopy) and RBS (Rutherford Back Scattering) measurements.

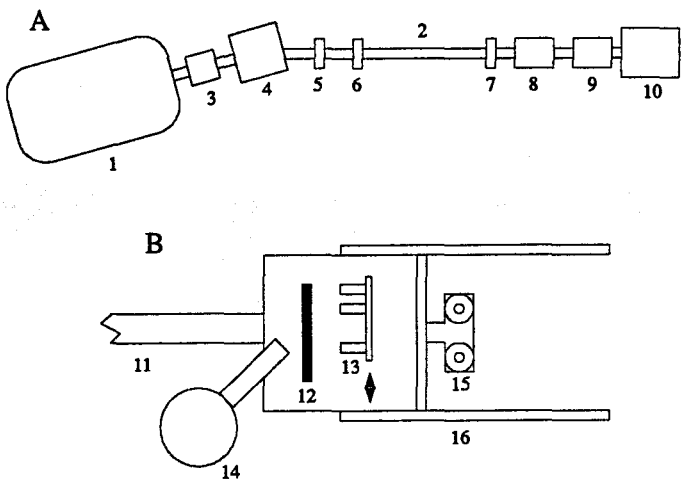

Figure 3.8: *Micro beam facility in Lund. A) Top view of the beam line B) detailed view of the chamber 1) van de Graaff accelerator 2,11) beam tube 3) quadrupole pair 4) switching magnet 5,6,7) slits 8) quadrupole triplet 9) scanning magnet 10) chamber 12) target wheel 13) moveable holder with Faraday cup, detector and objective 14) X-ray detector 15) microscope 16) pneumatic opening of the chamber*

3.2 Electronics

Different electronics setups are needed for the measurements. Different configurations are used for the ΔE-E telescope and the pulse shape analysis.

For the bias voltage of the detectors and the photo diode a Silena 7710 power supply is used. This supply can deliver a voltage up to 400 V. The internal current meter gives the bias current with a resolution of 1 nA.

To prevent ground loops that introduce noise and a DC offset in the signals, it is useful to use only one common ground for all electronics that are used. This can be done by using a ground-isolator for all electronics that are not directly placed at the data-aquisition system. This ground isolator consist of a 220 V to 220 V isolation transformer. This device was used for all measurements in Uppsala.

3.2.1 ΔE-E telescope

The electronics needed for a ΔE-E telescope are rather straightforward. The energy signals are amplified and fed directly into the ADC's. Also the timing signals are amplified, fed into a discriminator and a coincidence unit. The fast coincidence can be set this way from 40 to 600 ns. Since our ADC's only need a coincidence pulse during the conversion, no gate and delay unit is required.

3.2.2 Pulse shape analysis

For the pulse shape analysis (PSA), some extra electronic units are needed for converting the pulse shape into an analog signal.

Two different setups are used to do this conversion. The first setup was done with our own electronics. This was based around an ORTEC 552 pulse shape analyzer. The other setup is built and designed by M. Moszynski and was used during the cyclotron measurements.

Conventional electronics

Since we used most detectors in a ΔE-E configuration with the positive side of the detector towards the target (reversed placing), we had some possibilities to get more information than the pulse shape alone. Two different setups are shown in figure 3.9 and 3.10.

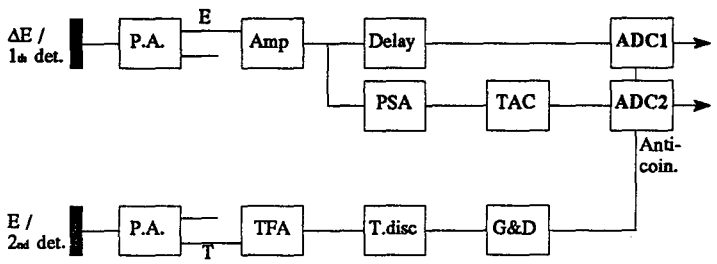

Figure 3.9: *Configuration for the pulse-shape analysis. PA) pre-amplifier PSA) pulse-shape analyzer TAC) time-to-amplitude converter TFA) timing filter amplifier T.disc) timing discriminator G&D) gate and delay generator*

The setup of figure 3.9 shows the electronics in the case that the first detector in the telescope is used for PSA. The energy signal is amplified, delayed and fed into the first ADC. This gives energy value. The PSA unit consists of two constant fraction discriminators. They are adjusted in such a way that they trigger at two different fractions. The two signals are used for starting and stopping a time to amplitude converter. This signal is fed into the second ADC and gives information about the pulse shape. Since PSA only works for particles that are stopped in a detector, the second detector is used as a veto detector. It has to be mentioned that the shortest shaping time the amplifier can be adjusted to is 0.25 μs. Remember that the carrier collection time in a reversed silicon detector is around 100 ns.

In the case that the second detector is used to perform PSA, the first detector can be used to get ΔE information. By making a three parameter (Δenergy, energy and pulse shape) measurement, one can have a double check on the the identification of the particles and in this way get more understanding of PSA (and that is after all the purpose of the measurements). Unfortunately, the analysis of three-parameter data cannot be done in real time.

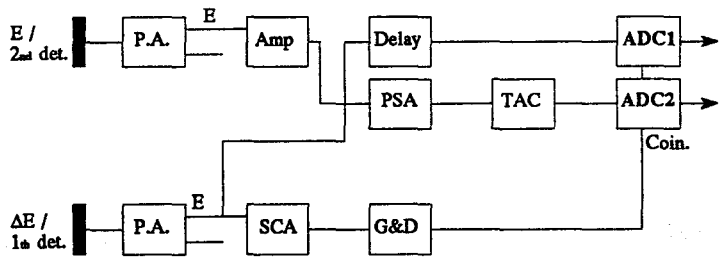

Figure 3.10: *Configuration for the pulse shape analysis to obtain a Δ E-E plot. PA) pre-amplifier Amp) amplifier PSA) pulse-shape analyzer TAC) time-to-amplitude converter TFA) timing-filter amplifier T.disc) timing discriminator G&D) gate and delay generator SCA) single channel analyzer*

Therefore I came up with another configuration, where the measured pulse shape can be directly seen as a function of the incoming ion. It is shown in figure 3.10. Instead of taking a full three parameter measurement, a single channel analyzer is used to 'select' an energy channel. Since the energy is known from the SCA, the two parameter plot is directly a slice of a three dimensional measurement.

M. Moszynski's electronics

M. Moszynski and D. Wolski have designed and built their own pulse-shape analyzer. A diagram [CHM95] is shown in figure 3.11.

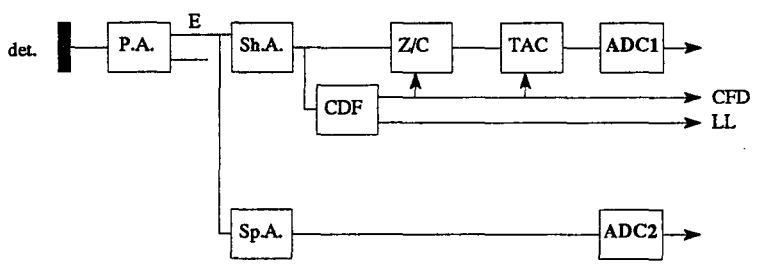

Figure 3.11: *Configuration for the pulse-shape analysis used by M. Moszynski. PA) pre-amplifier sh.Amp) shaping amplifier sp.A) spectrum amplifier CDF) constant-fraction discriminator Z/C) zero-crossing filter TAC) time-to-amplitude converter*

For starting the TAC they use also a constant-fraction discriminator. However, for the stop signal they use a zero crossing filter. But this is not the main difference compared to our own experimental set-up. The shaping amplifier has a shaping time that can be switched between 100 and 150 ns. This matches the carrier collection time of a reversed detector.

3.3 Data-acquisition

A typical event rate for nuclear experiments is between 100 and 10000 events per second. Therefore computer systems are used for the acquisition. I have used two different systems; An IBM-PC based Multi Parameter (MP) system manufactured by Canberra and an Apple based Sparrow system.

3.3.1 MP system

The Canberra MP system consists mainly of three parts. The main electronics are placed on a board that is put inside a PC. A box with electronics converts the ADC data to the proper signals for the PC-card and computer-program displays and stores the data. The PC itself has a 33 MHz 486 DX processor, a 250 megabytes harddisk and a QIC-80 based tape drive to backup the data. The PC also contains an ethernet card to connect the system to the rest of the world. The PC is mounted with a NIM crate on a cart, so it can be easily transported to the different experimental setups.

The functions of the PC-board are centered around 2 megabyte RAM. This is used for temporary storage of the data without interference of the PC (and without laying a claim on the system resources).

The data can be acquired in three different ways. The first method is called the 'single independent' mode. This mode is similar to the 'histogram mode' in some other systems. Here, just histograms are made from all input channels. The number of channels can be chosen for each input between 32 and 8192 (in powers of two). Since the PC-board does all the acquisition work, the PC can use its power fully to display the data or to fit gaussian shaped curves at the measured peaks. The second mode is the 'multi parameter mode'. In this case, a multi dimensional histogram is made. Each channel (counter) of the histogram can consist of 1, 2 or 4 bytes. Also the number of channels can be set up for each input channel. So the board can be adjusted for optimal use of the 2 megabyte of memory. On board there is also a (slow) coincidence unit with a coincidence time between 0.35 and 16.1 μs. This coincidence unit works with the analog signals. (to be more accurate, it compares the times when the analog to digital conversion were completed) The software can display one or two parameter projections of the multiparameter histogram. The two parameter projection can be displayed as a 'flat model', where the colors give the indication for the number of counts. Also a semi three dimensional wire frame can be produced. The last mode is the 'list mode'. All data of the input channels are just stored in memory as 16 bit words. The least significant 13 bits contain the ADC value and the highest 3 bits the ADC number. The data is stored in blocks on harddisk.

The maximum number of ADC's (or other digital input devices like multi channel scalers) one can attach to the system is determined by the conversion box. Our system could have a maximum of 3 ADC's, but this can be expanded to 8 ADC's.

The ADC's we mostly used for the experiments are two Canberra 8085 13 bits ADC's. We also tested two borrowed 8087 ADC's. They are supposed to be faster. They give a slightly (few percents) better resolution.

3.3.2 Sparrow

The Sparrow systems consists of an Apple Macintosh 650 computer, Kmax software and a CAMAC interface. The Kmax software allows the user to configurate the system, control the measurements and show the measured data with the graphical interface of the Macintosh. For every electronical unit, one can write or buy so called software modules, that contain all software that is needed to communicate with the unit. This communication is done by a board that is placed inside the Macintosh and a 39922-Z1B parallel bus crate controller, made by Kinetic Systems. For the

multiparameter data acquisition, display, sorting, analysis and reporting, we used the HAWK 3 system, made by Sparrow. It requires an ORTEC HM413 histogram memory and a AD413A QUAD ADC.

This system was only used during the measurements in the gamma cave for the pulse shape analysis.

3.3.3 Microbeam data-acquisition system

The system used for the microbeam facility in Lund is built around a Microvax II connected to a VME bus. Both the scanning magnets and the the ADC output is connected to the VME bus. The scanning pattern is limited by the analyzing software. The options for a surface scan is 64 x 64 pixels or 128 x 32 pixels. The number of points for a linescan is only limited by the used DAC's. The maximum scanning frequency is 60 Hz. The acquisition of the data can be done as well in histogram mode as event (list) mode. In both cases the real time monitoring of the measurement is done at the microvax system.

There are plans to change the system to a Sparrows system in the future.

Chapter 4

Silicon ΔE-E telescope

A ΔE-E telescope consists of a thin first detector which is followed by another thicker detector. In the CHICSi telescopes, the first detector will be a 10 μm silicon detector. A 300 μm detector is chosen as thick detector. A third (300 μm) detector is mounted to detect particles that were not stopped in the telescope and would therefore otherwise contribute to the background. All these detectors have an active area of 9.5 x 9.5 mm. The lower limit in energy for the detected particles is directly related to the thickness of the thin detector. For a 10 micron detector this lower limit is around 0.8 A MeV. The upper level is related to the total thickness of the telescope. This is around 6 A MeV.

4.1 Characteristics of the telescope

To obtain a good mass and energy resolution with the telescope, the individual detectors that form the telescope should have several characteristics.

- The energy resolution of the detectors should be sufficiently low to guarantee full mass separation when placed in the telescope.
- The uniformity in resistivity has influence on the energy resolution and therefore need to fulfil the demands in the previous point.
- The uniformity of the thickness of the thin detector should be below 0.5 micrometer. Otherwise one does not know what the exact energy loss in this detector is. This will affect the mass resolution.
- It is very important to know how the detectors stand radiation damage and how this affects the (energy) resolution.
- A great problem for thin detectors is the high capacity they have. This will introduce a high electronical noise in the preamplifier.
- A problem that is related to the high capacity is that a detector picks up the RF structure that is used in storage rings to accelerate the particles. I will further refer to this effect as 'pick up'.

Two companies were given an order to develop and to deliver a batch of test detectors with a thickness of 10 and 300 μm. These two companies are SINTEF and Micron. SINTEF will also make the integrated circuit that will be put at the detectors for the read out. Only SINTEF did deliver some prototypes of the thin detector. We have used two versions. The main difference is that the older version does not have guard rings. Guard rings lower (when a suppressor voltage is applied) the leakage current. The detectors have an active area of 9.5 x 9.5 mm and an outside area of 11 x 11 mm. They are delivered as chip and have to be mounted and connected before they can be used.

4.2 Experiments

For testing the SINTEF detectors several tests were performed. The resistivity uniformity was tested in the small detector chamber. For testing the mass resolution, measurements were performed during 18 shifts of 8 hours at the tandem and for 48 hours at the cyclotron. The micro beam facility in Lund was used to look at the thickness variation and the response of the detector on this thickness variation. Also some tests were performed using a 13 μm p-type detector that was made by V. Avdeichikov from Dubna. This measurement was done to obtain data that can be used for comparison with the SINTEF detectors.

4.2.1 Mass resolution and radiation damage

The first test with a telescope that consists of SINTEF detectors was done in December 1994. This telescope was made with detectors of the old design. Unfortunately, both thick detectors in the telescopes did not work. The leakage current was very high and was only limited because of the resistor inside the pre-amplifier. The signal out of the detector consisted only of a high noise signal (compared to a normal detector) and no particles of the α-source could be seen. Since the shieldings in the chamber were not placed by then, it could have been that the detectors were hit by the beam during beam alignment.

Gamma cave experiments

In the gamma cave test in the beginning of February we had new detectors delivered with the new design. Tests with an α-source had already showed that the thin detector was 16 μm thick.

The telescope consisted of three detectors. The first detector was a thin detector followed by two thick ones. The last detector was used as veto for particles that are not fully stopped in the first two detectors. The used reaction was 450 MeV ^{14}N on ^{124}Sn. The result of one of these measurements is shown in figure 4.1. Although the veto detector was present, some punch through is still visible. One can observe isotope separation for ^{7}Be and ^{9,10}Be. In [LAV89] other measurements are shown with the same reaction.

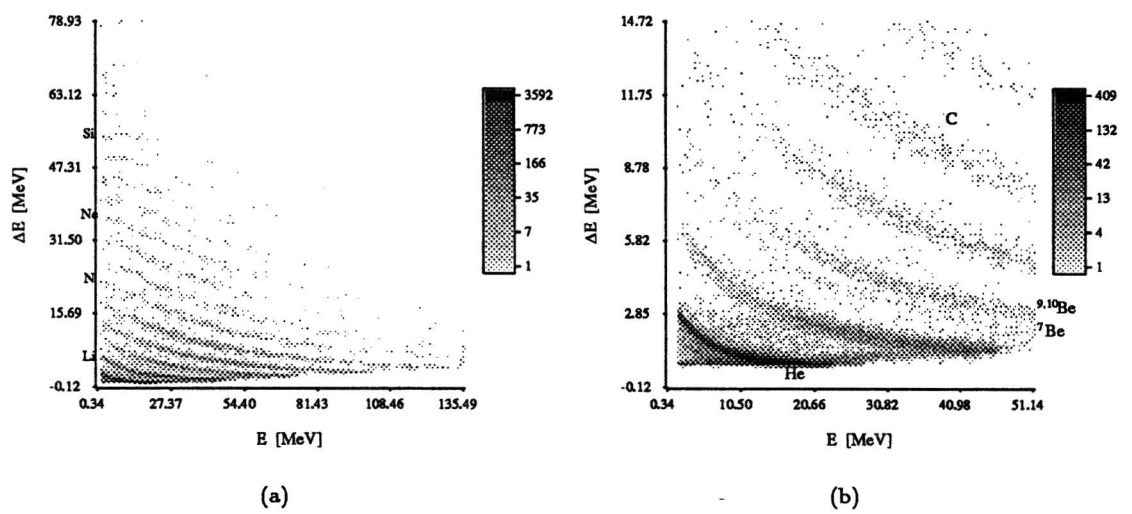

Figure 4.1: *ΔE-E plot of the measurement at the gamma cave with the SINTEF telescope a) all events b) the light ions*

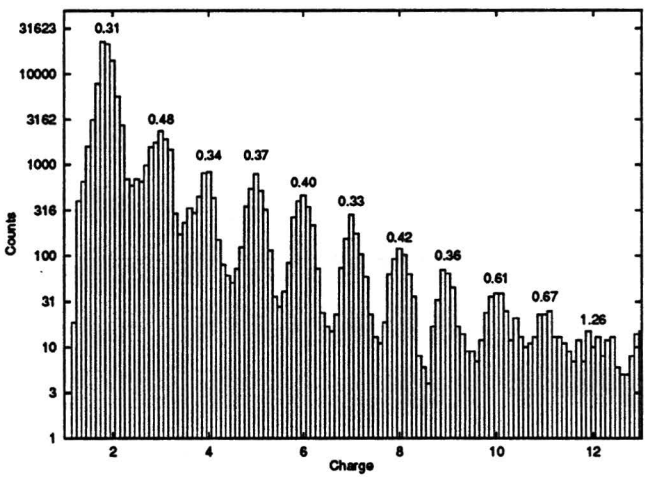

Figure 4.2: *Atomic number plot of the measurement done with the SINTEF telescopes in the gamma cave. The numbers in the atomic number plot indicates the FWHM of the peak.*

The atomic number spectrum is given in figure 4.2. The way this spectrum is calculated is explained in section 4.4.

In the last three tests at the tandem, we have used a telescope that consists of the new design of SINTEF detectors. The leakage current is according to the manufacturer only 200 pA. (Since our current meter has a resolution of 1 nA, we cannot see this current)

Because we saw a high leakage current at the earlier tests at the tandem, we did the following test to see whether the detector could stand air and vacuum when a bias voltage was applied. The thin detector was mounted and the leakage current was measured for 12 hours in air. The next 12 hours it was placed in vacuum followed by 12 hours irradiating with an α-source (50 particles/s). No raise in bias current could be seen (that means actually that the bias current stayed below 1 nA).

Tandem test

During the tandem test in March 1995, we have used 7 thin and 2 thick detectors. The used beam was 44 MeV ^{16}O on three different targets. The ΔE-E measurements and the atomic number spectra for a 200 $\mu g/cm^2$ aluminium foil, a 130 $\mu g/cm^2$ carbon and a melamine (H_2NCONH-CH) foil with a carbon backing can be seen in figure 4.3 to 4.5.

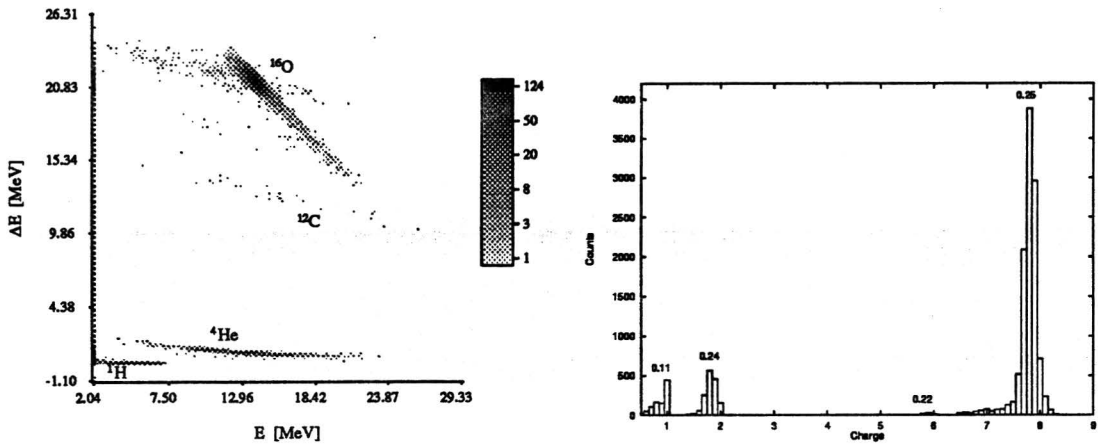

Figure 4.3: *ΔE-E plot and the calculated atomic number spectrum of the measurement at the tandem with 44 MeV ^{16}O on aluminium. The numbers in the atomic number plot indicates the FWHM of the peak.*

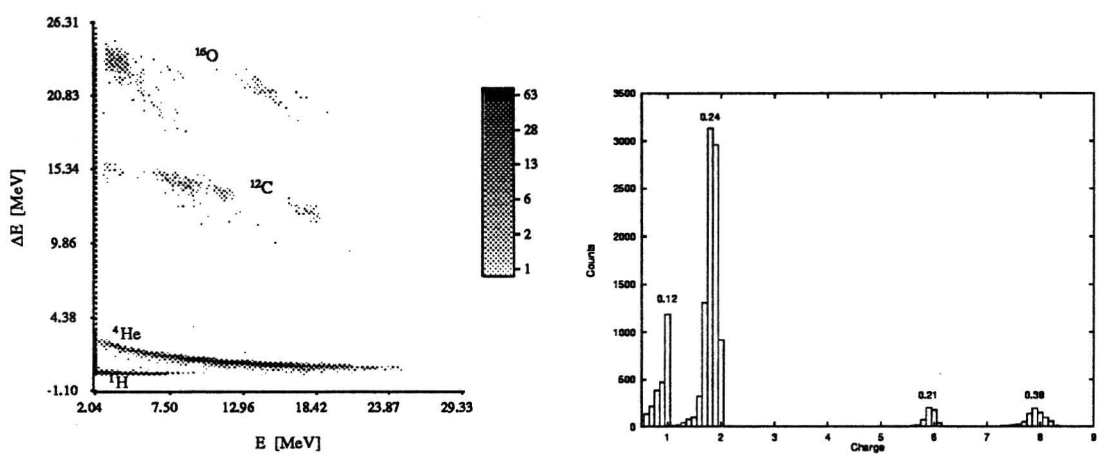

Figure 4.4: *ΔE-E plot and the calculated atomic number spectrum of the measurement at the tandem with 44 MeV ^{16}O on carbon. The numbers in the atomic number plot indicates the FWHM of the peak.*

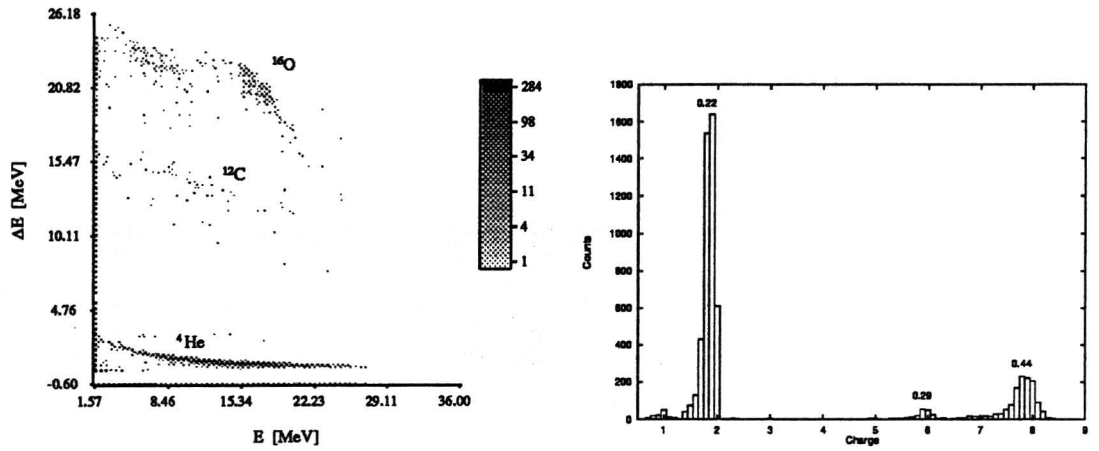

Figure 4.5: *ΔE-E plot and the calculated atomic number spectrum of the measurement at the tandem with 44 MeV ^{16}O on melamine. The numbers in the atomic number plot indicates the FWHM of the peak.*

Unfortunately, all 7 detectors could not stand the test. The problem did arise with the leakage current. A typical leakage current-dose plot for a measurement with aluminium target is given in 4.8. In this case the dose is calculated by looking at the number of events at the data-acquisition system and by monitoring the signal of both detectors on the oscilloscope. A higher event rate is observed at the thick detector since high energy protons cannot be seen in the thin detector (the pulses disappear in the noise). Also to make sure that the increase in current was really caused by the particles we stopped the beam several times to make sure that the leakage current stayed then constant. All detectors were damaged after around 10^6 particles/cm^2

A remarkable thing is that the energy resolution is the same for a new detector as for a 'damaged' detector. The thin detector only needs a bias current of 6 V. Since the internal resistance of the pre-amplifier is around 100 MΩ, a leakage current of 60 nA just means that the complete voltage fall is at the resistor and the detector has no bias voltage any more. But the thin detectors are almost completely depleted (no decrease in noise can be observed when applying the bias voltage) without any voltage (see equation 2.16). This can explain that the resolution stays the same when the detector is damaged.

Different pre-amplifiers give different bias currents for the same damaged detector, because of the internal resistance:

Pre amplifier	Leakage current
Intertechnique (1)	34
Intertechnique (2)	64
Ortec 142B (1)	37
Ortec 142B (2)	75

Also have we placed a 200 μg/cm^2 aluminium foil in front of the telescope. This gave a slight decrease in the leakage current raise. An important thing is that only the thin detector was damaged. Also the detector telescope that was used in the gamma cave (and therefore have had at least a dose of $5 \cdot 10^7$ particles/cm^2, without a leakage current raise) was damaged when it was tested in the tandem chamber.

After this test we have made several hypotheses for the cause of the damage.

- The particle-detectors just cannot stand many particles.
- The expected particles for the different targets are given in appendix C. Most of the low energy recoils from the targets are stopped in the thin detector. Especially aluminium and nitrogen (in melamine) can act as acceptor or donor in a silicon semiconductor. This can destroy the diode (and that is all a silicon detector is). But the concentration (although most particles are stopped in a thin layer) is small (few orders of magnitude) compared with the doping concentration.
- Delta electrons are electrons that are dragged by the ions in (for example) the target. These electrons have the same velocity as the ions (and therefor a fraction of the energy). These delta electrons can induce chemical reactions. Since the electrons have an energy around a few keV, they can not be observed in the detectors.
- The passivated layer, that protects the silicon from oxidising and reduces the bias current, can be damaged by the lower energy ions (and therefore have a high nuclear stopping power) or by the delta electrons.

For testing whether the detectors could stand particles at all, we radiated the telescope with a ^{241}Am α-source with a 180 particles per second. At a dose of $2.2 \cdot 10^8$ particles/cm^2, the leakage current of the thin detector was not increased. The leakage current of the thick detector had an increase of 2 nA.

For testing the hypothesis about the doping, we changed the beam to 49.5 MeV ^{19}F. Also, only a ^{12}C and a ^{9}Be target were used. It has to be mentioned that berilium always has an oxide layer. In appendix C is shown that when the detector is placed at 42^o, no scattered fluorine will reach the detector and the recoils can pass the thin detector. The ΔE-E plots and the atomic number spectra are shown in figure 4.6 and 4.7.

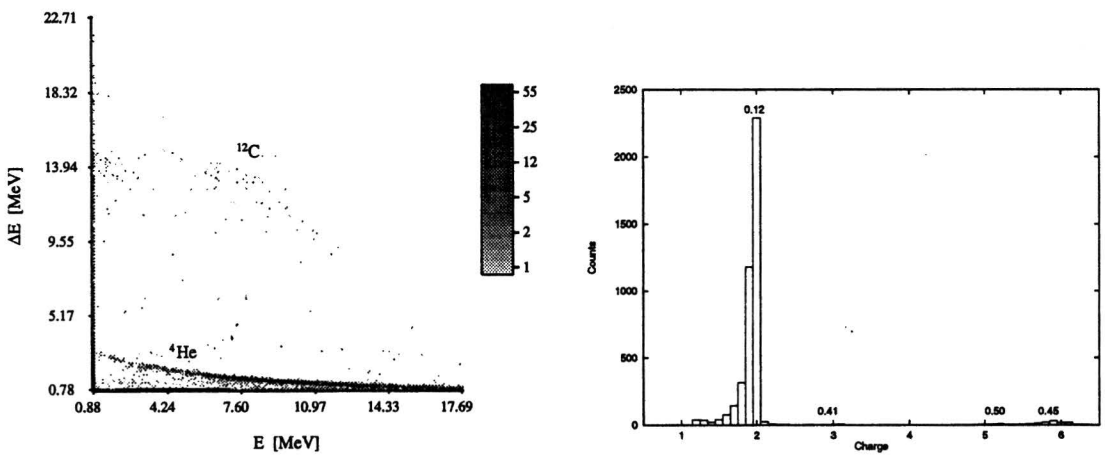

Figure 4.6: *ΔE-E plot and the calculated atomic number spectrum of the measurement at the tandem with 50 MeV ^{19}F on ^{12}C. The numbers in the atomic number plot indicates the FWHM of the peak.*

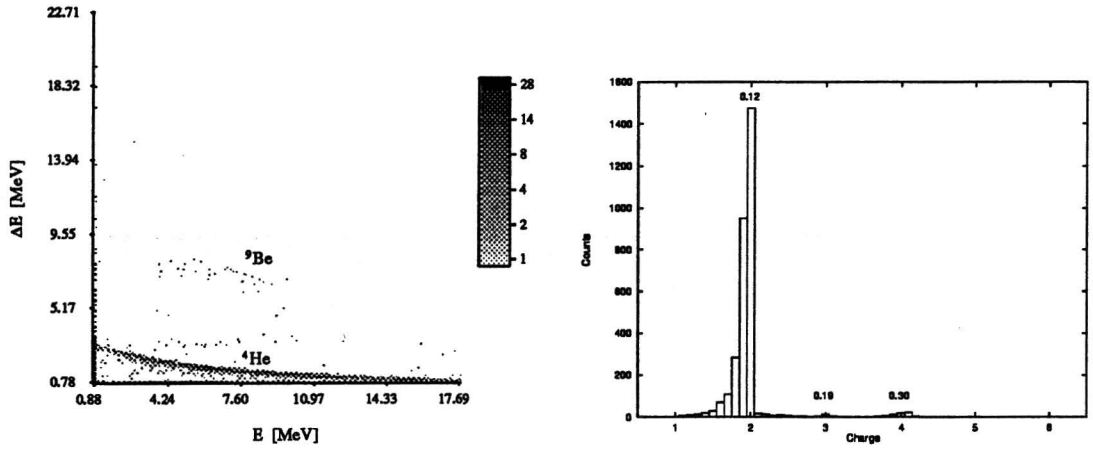

Figure 4.7: *ΔE-E plot and the calculated atomic number spectrum of the measurement at the tandem with 50 MeV ^{19}F on ^{9}Be. The numbers in the atomic number plot indicates the FWHM of the peak.*

Also now, the detector got damaged. A graph of the leakage current is shown in figure 4.8.

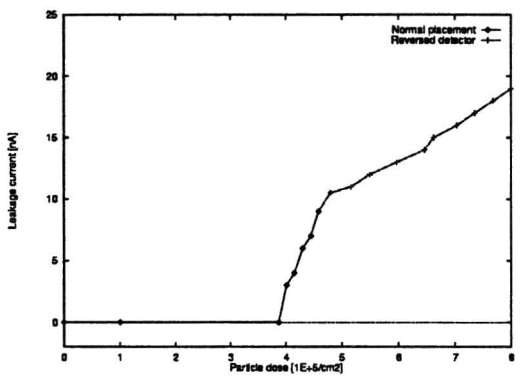

Figure 4.8: *Leakage current versus the dose for the thin detector with 50 MeV ^{19}F on ^{12}C and ^{9}Be. Also a thin foil was placed in front of the detector. The detector had a collimator with a diameter of 4 mm. The dose is converted to particle/cm^2.*

In all tests the thick detector has been covered by the thin detector and it did not get damaged. So we decided to test the thick detector without a thin one in front. Due to a failure in the accelerator, we only could get 43.5 MeV fluorine ions. Surprisingly, the thick detector was also damaged. Reversing the direction of the detector showed a slower increase in leakage current. A graph of the current is shown in 4.9. The bias voltage is 57 V and the leakage current for a new detector is (according to SINTEF) 200 pA.

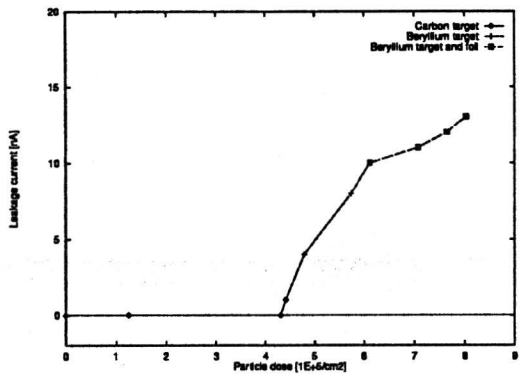

Figure 4.9: *Leakage current versus the dose for the thick detector with 44 MeV ^{19}F on ^{12}C. The detector had a collimator with a diameter of 4 mm. The dose is converted to cm^{-2}.*

α-Source test

To compare the sensitivity for radiation damage between the SINTEF and Micron detectors, two 300 μm detectors (from SINTEF and Micron) were placed in the tandem vacuum chamber with a ^{241}Am source in front. The counting rate was for the SINTEF detector 2150 particles per second (on its entire active area) and for the Micron 2550 particles per second. The SINTEF detector has at the beginning a leakage current below 1 nA, while this value for the Micron detector 63 nA was. The observed increase in leakage current was:

Detector	Increase [nA]	Dose [particles]
SINTEF	25	$3.8 \cdot 10^8$
Micron	18	$4.1 \cdot 10^8$

The increase in leakage current for the Micron detector was 46 nA after $8.6 \cdot 10^8$ particles.

4.2.2 Micro-beam test

At the micro beam facility in Lund, we have performed a Scanning Transmission Ion Microscopy (STIM) measurement on the thin SINTEF detector (to avoid confusing with the real detector in the experiment, the SINTEF detector will be called 'sample'). The used proton energy was 1.2 MeV. It was chosen this way because then around half of the energy is lost in the sample. The energy resolution of the detector was 14 keV (measured with the direct beam).

During a STIM measurement, ions lose energy in the sample. The remaining energy is measured and gives information about the sample. To get the average energy loss in one point, I have used Chauvenet filtering. First the average of the energy ($\bar{E}$) of all events of one point and its standard deviation (SD) is calculated. Then, the same thing is done again, but now only all events with an energy of $\bar{E} \pm 128 \cdot SD$ are taken into account. This is done over again with $\bar{E} \pm 64 \cdot SD$, $\bar{E} \pm 32 \cdot SD$ etc. until $\bar{E} \pm SD$. Now $\bar{E}$ is supposed to be the average remaining energy. The thickness can be calculated with the range formula as described in chapter 2.1.

We have done two kinds of measurements. First we have made a 6 x 6 scan over the whole surface (9 x 9 mm), with a beam of 3 μm diameter. Since the detector only has an area of 3 x 3 mm, the sample has to be moved (with the stepping motors) by hand over the surface. The result of this measurement is shown in figure 4.10 as a the thickness variation for a horizontal line through the center and for a diagonal scan.

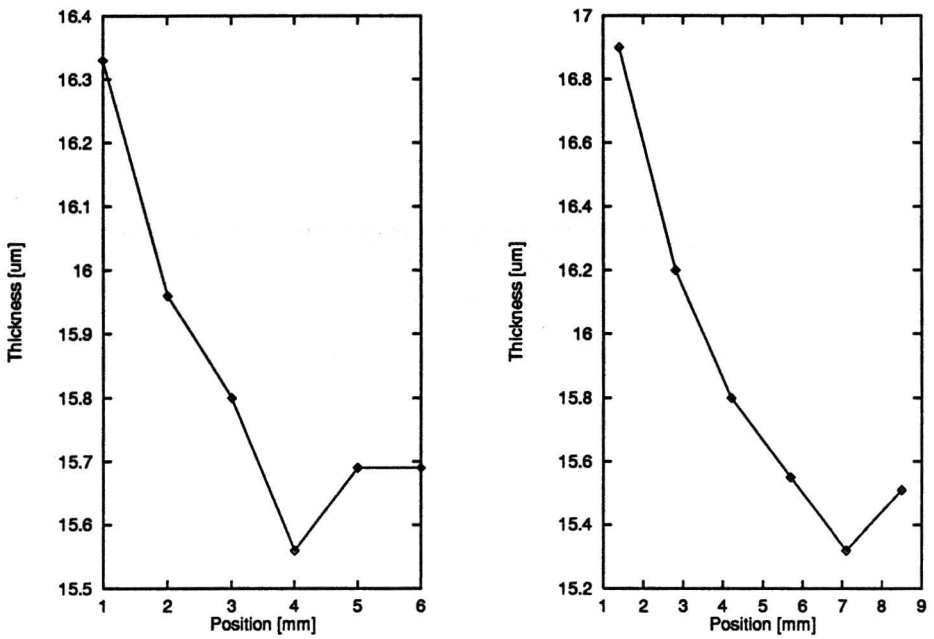

Figure 4.10: *Thickness of SINTEF '10 μm' detector for a line (a) through the center and diagonal (b).*

Also a surface scan of 64 x 64 points with a step size of 3 μm is performed in the middle of the sample and on a corner. The result is shown in figures 4.11

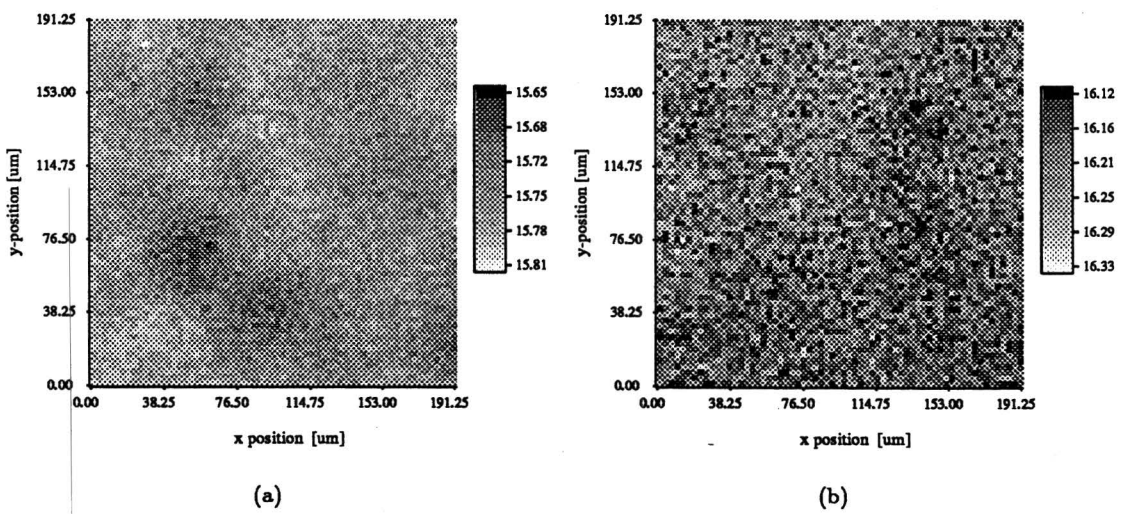

Figure 4.11: *Thickness variation in the middle (a) and at the corner (b) of the SINTEF detector. The scanned area is 192 x 192 μm in 64 x 64 points. The thickness is given in μm.*

Measurements were performed with the SINTEF detector (the sample) connected and read out. This gives a relation between the energy loss of the ion in the detector and the signal it produces. We have called this technique Active STIM. This technique will also be used to look how much energy it costs to create electron-hole pairs, and whether this is dependent on the initial energy of the ion.

Unfortunately, due to some faults, no accurate calibration was available. This measurement has therefore to be done again later.

4.2.3 Pick up test at CELSIUS

The CELSIUS ring is a combination of an accelerator and a storage ring. For accelerating an injected beam, a RF structure is applied. Since a detector has a certain capacity, it can pick up this RF structure. This will increase the noise.

Two Intertechnique passivated ion implanted silicon detectors with a thickness of 300 micrometer were placed at 135 degrees at the CELSIUS reaction chamber. A ^{241}Am source on a bended copper strip was placed in between the detectors for calibration purposes.

The experiment was done during a run of the CA01 group. They are studying excitations of giant resonances by using 4 GeV ^{16}O on a ^{40}Ar gas target. A result of a Δ E-E plot can be seen in figure 4.12.

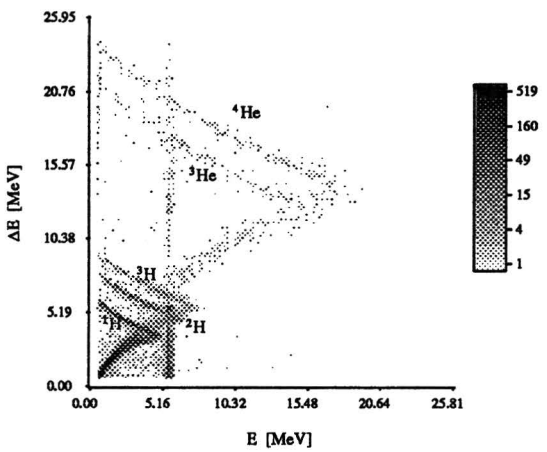

Figure 4.12: *ΔE-E plot of 4 GeV ^{16}O on ^{40}Ar reaction with the detector at 135°. the vertical line at 5.4 MeV is caused by the α-source.*

For the determination of the pick up, an oscilloscope was used. No RF pick up could be seen in the energy signals. But using a Phillips 775 fast rise time amplifier (with a rise time of 20 ns), the RF signal could be seen in the timing signal and looked like 60 ns pulses that repeat themselves every 200 ns. Although it is not normal to speak about resolutions in the timing channel, it gives a good indication what the magnitude of the pick-up is.

The pick up in the timing channel was 525 keV, while the noise (when there was no RF structure) was 415 keV. Two things have to be mentioned.

- A 300 micrometer detector has roughly a capacity that is 30 times lower than a 10 micrometer detector (33 nF / 1000 nF).
- Earlier experiments show that a doubling of the risetime decrease the noise with 40 %.

4.2.4 V. Avdeichikov's detector

To have some data to compare the SINTEF telescope with, we have used a ΔE-E telescope at the tandem that consists of a 13 μm p-type detector made by V. Avdeichikov from Dubna, Russia and an Ortec 138 μm detector. The leakage current of the thin detector was 20 nA at 9 V. The calibration was done with a ^{241}Am source. The used reaction was ^{16}O on ^{27}Al and ^{12}C. The ΔE-E plots and the mass resolution are given in figure 4.13 and 4.14.

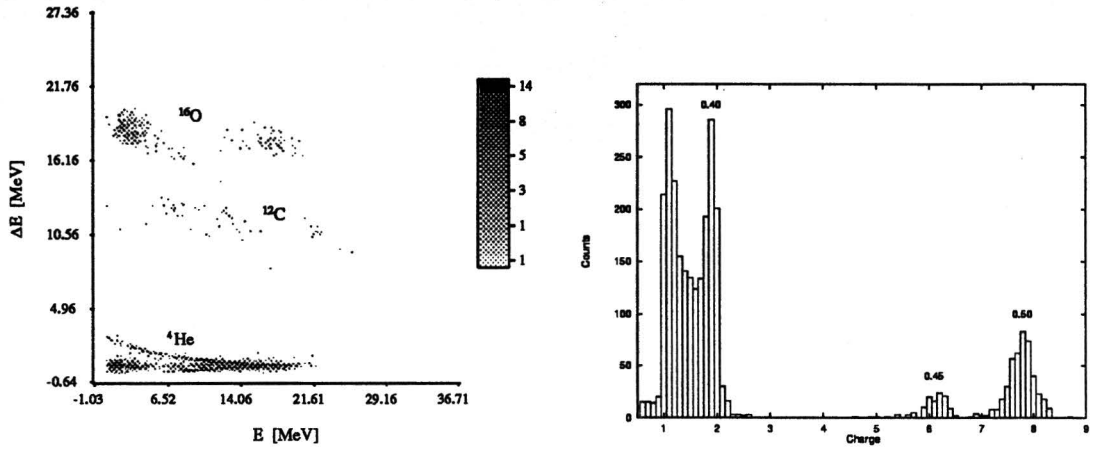

Figure 4.13: *ΔE-E plot and the calculated atomic number spectrum of the measurement at the tandem with 40 MeV ^{16}O on ^{12}C. The numbers in the atomic number plot indicates the FWHM of the peak.*

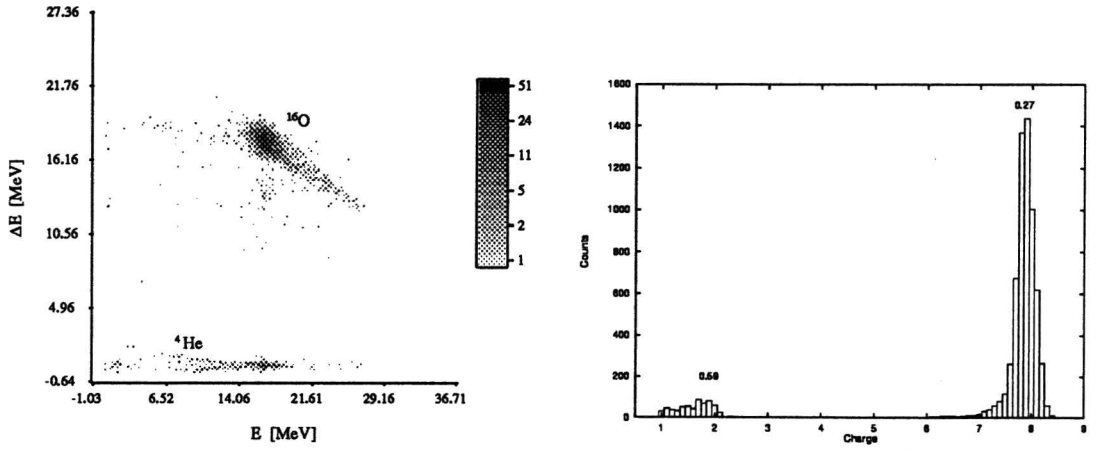

Figure 4.14: *ΔE-E plot and the calculated atomic number spectrum of the measurement at the tandem with 40 MeV ^{16}O on ^{16}O. The numbers in the atomic number plot indicates the FWHM of the peak.*

4.3 Channeling

In figure 4.15, a ΔE-E plot is shown with the projected ion curves. It is the same measurement as displayed in figure 4.3. The scattered oxygen ions form a spot in this figure. One can observe a certain tail from this spot, with events that has deposited less energy in the ΔE detector and more energy in the E-detector. The total energy is however the same as the energy of the recoils. This effect is due to < 111 > channeling in the thin detector ([AVD95]). It is possible to calculate with equation 2.14 the critical angle for ions to channel. Not all ions that fall into the detector with an angle lower than the critical angle will channel (see section 2.1.3). An estimation can be made what part of the infalling particles will channel. Since the detector was placed 20 cm from the target, only 0.2 % of the particles could channel. The number of channeled particles in figure 4.15 for the scattered oxygen beam is 5 %. Remember that some detectors in the final CHICSi telescope only have a distance of 5 cm to the target. In that case the part of the ions that will channel is much higher.

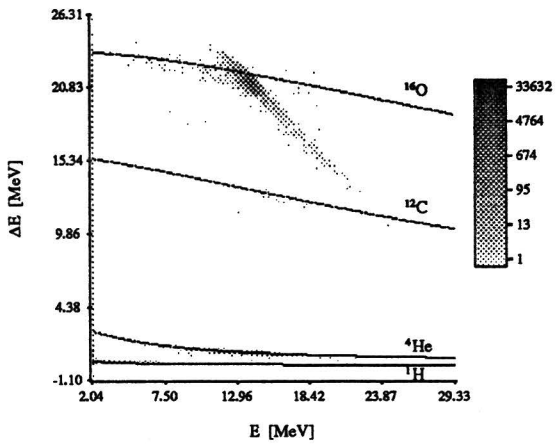

Figure 4.15: *ΔE-E plot with the projected ion-curves*

4.4 Calculation of the atomic number spectrum

To resolve the mass resolution of a mass-analyzing telescope, the measurement (the ΔE-E histogram) has to be converted to a mass spectrum. This is done mostly by using the Bethe-Block formula (equation 2.1). This formula gives the stopping of an ion in matter. This can be used to calculate the energy loss in the thin detector in the telescope. This method does not give the mass of the incoming ion, but the value $(\frac{1}{2}AZ^2)^{\frac{1}{3}}$, with A and Z the atomic mass and charge. The disadvantage of this method is that the Bethe formula has to be adjusted for the different ions.

Therefore, I have used another method, that uses range data. I have written the program in Pascal. Instead of giving the mass spectrum of a measurement, it gives the atomic number spectrum.

The main concept of this method is that a computer program calculates the ion curves in a ΔE-E plot and with that information identifies the atomic number of the ion that caused the event. Therefore it is very useful to check the calibration by projecting the ion-curves at the ΔE-E plot. An example is given in figure 4.15. In figure 4.16, two possible events are shown (1 and 2). The first thing that the program does, is to calculate the total energy that the ion had (this is the energy in the thin detector added with the energy in the thick one). The program has a table which gives the mass of each atomic charge. It calculates for the different atomic numbers how much energy such an ion would have deposited in the thin detector. It will find two successive atomic numbers which ions would have given more and less energy in the thin detector (point 3

and 4 in the figure). The combination of the atomic numbers and the deposited energy gives the virtual atomic number.

There are two problems. The first is shown in figure 4.16 at event 2. Here, the ion with the higher atomic number will not pass the thin detector any more (and gives only the energy as in point 5). Now, not point 5 is taken to calculate the atomic number, but point 7, that corresponds to an ion that had the minimum energy to pass the thin detector.

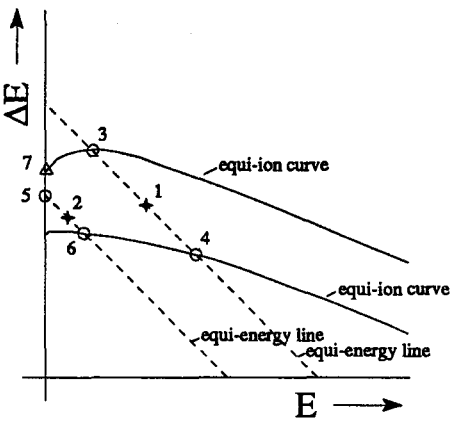

Figure 4.16: *ΔE-E plot with two possible events.*

The second problem is caused by events that fall under the proton curve. Therefor one has to assume that there is a zero charged particle that does not give any energy in the thin detector.

There are two phenomena that have a bad influence on the atomic number plot. Punch through (visible as tails at the ion curves) cannot be distinguished from noise. These events will look like events that were caused by ions with a smaller atomic number. Another problem is when a curve is cut off at the bottom of a plot. In that case, the distribution of events that will be seen as lower and higher atomic number, is not equal anymore.

The Full Width Half Maximum (FWHM) of the peaks in the atomic number plot is calculated by fitting a Gaussian shaped function at the peak with a least square fit.

4.5 Conclusion

A ΔE-E telescope built with SINTEF detectors gives full mass separation for all ions we have observed during our experiments (up till ^{40}Ar). The atomic number resolution lays for these telescopes around 0.4 amu. This is comparable with the mass resolution that we have measured with a telescope that contained a high quality p-type detector.

Unfortunately, the SINTEF detectors are not stable and are very easily damaged by radiation. The damage is formed by a dramatic increase of the leakage current. The energy resolution is not affected by this damage. It is the question whether this increase in leakage current is special for our detectors. Normally, the leakage current is not measured as accurate as we have done ([WHIPC]) and the increase is only well visible, because of the leakage current for a fresh detector is very low (200 pA) compared to normal detectors (> 50 nA). Also the detector that is manufactured by

Micron shows the same instability as the SINTEF detector.

The micro-beam tests show that the microscopic thickness variations are below 0.2 μm. This is better than the requirements (0.5 μm). The overall variation however is disappointing. According to SINTEF is that only a problem with the prototype (since the masks were used for different projects).

There has to be done more tests on the influence of the RF-structure in the CELSIUS ring on the noise level in the thin detectors. It is not clear of what magnitude the pick-up will be and whether it can be diminished by turning the detectors around.

Channeling in the thin ΔE detector creates a background in the measurement. Although only a small part (< 1 %) of the particles have a chance to channel, it could be a good idea to fabricate the detectors with an angle around 4^o out of the crystal axis ([AVD95]).

Chapter 5

GSO ΔE-E telescope

As mentioned before, several detectors will consist of three active detectors. The first two detectors is the same pair as used in the other telescopes. As third detector a cesium doped GSO-scintillator crystal is used (Gd_2SiO_5), with a thickness of 6 mm and an area of 10 x 10 mm. This stops protons up to 60 MeV. This crystal has a peak emission at 430 nm. The readout of the scintillator is done by a photo diode. This will probably be a naked Hamamatsu S3590-03 chip. As can be seen in [AVD94], the emission spectrum of the GSO crystal lies in the spectral response of the diode. The reason for use of a photo diode instead of a photo multiplier tube is that the final CHICSI telescope has to be compact. Also, photo diodes are easier to contact in ultra high vacuum.

5.1 Characteristics of the telescope

The noise level of a pin photo diode is lower than comparable surface barrier detectors due to their lower capacity. Noise levels around 4 keV can be obtained. However, a scintillator crystal does not convert all the ion's energy into light output. For a GSO crystal the efficiency is below one percent (that is only 12 to 16 % of the efficiency of a NaI crystal).

Furthermore, there is a loss in the transition from the crystal to the diode. This can be reduced by a light transmitting glue or oil. But until now, nothing is found that fulfil the ultra high vacuum requirements. The alternative is a vacuum gap of 150 micrometer. But this will introduce a loss around 20 %. A measurement was done by V. Adveidikov and is described in appendix G.

There is another problem that is caused by the volume of the crystal. Since the GSO crystal is located around 7 cm from the target, there will be particles that will leave the crystal through its side, without delivering all of its energy to the crystal. This contributes to the background.
photo diode was done with an α-source at the tandem. The whole telescope was tested in February 1995 in the gamma cave.

5.1.1 Tandem test

At the tandem a single spectrum was taken of the 60 keV γ-line of a ^{241}Am source. The bias voltage on the diode was 30 V. Ortec 142B pre-amplifier and 672 amplifier were used. Remember that 60 keV in the photo diode corresponds to (at least) 6 MeV protons in a GSO crystal.

The resolution in the energy signal was for different rise times:

risetime [μs]	resolution [keV]
4	6.0 ($\pm$ 0.2)
2	8.4 ($\pm$ 0.2)

The rise time is the time between the 10 % and 90 % level of the pulse.

No signal could be seen in the time signal. The noise level (directly from the pre amplifier) was 2 mV and that should correspond to 140 keV. This means that no normal timing electronics can be used for triggering purposes.

5.1.2 Gamma cave

A test with the complete GSO telescope was done in the beginning of February in the gamma cave. A 450 MeV ^{14}N beam from the Gustav Werner cyclotron was pointed at a ^{124}Sn target foil. As ΔE detector we used a 320 μm thick silicon detector. The GSO crystal was 10 x 10 x 10 mm and was covered by a foil that consists of aluminium evaporated on teflon to reflect the light pulse to the diode. The photo diode was a Hamamatsu S3590-05 chip that has an epoxy window. The photo diode was mounted with vacuum grease as optical medium.

Two configurations were used. The first measurements were done with a copper collimator with a hole of 9 x 9 mm and 5 mm thickness. The other measurements were done without collimator.

The measured data is used for several purposes. First of all, the effect of the collimator can be seen by looking at missing particles. This can be used in correlation with the Monte Carlo simulation done for this purpose. The other important thing is to look at the light output relation for the GSO crystal.

The Δ E-E plots for those measurements are shown in figure 5.1 to 5.3.

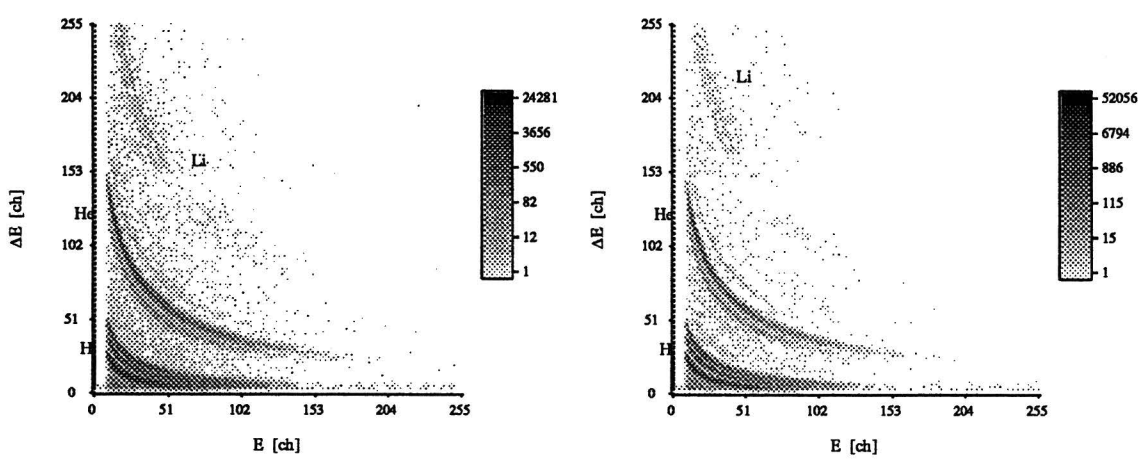

Figure 5.1: *ΔE-E plot of the measurement done to look at the effect of a collimator. a) with collimator b) without collimator*

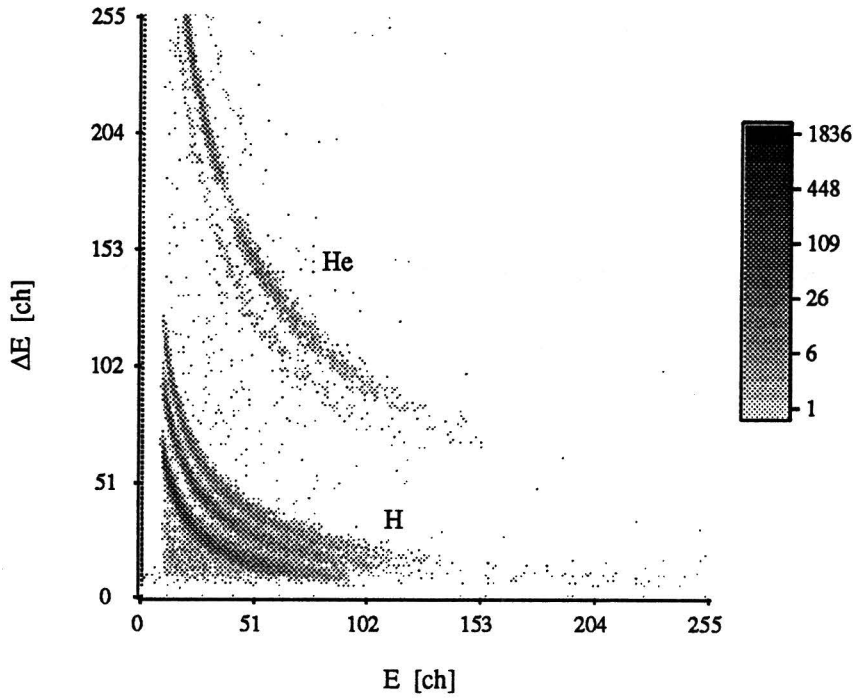

Figure 5.2: *ΔE-E plot of the measurement done to look at the light output relation.*

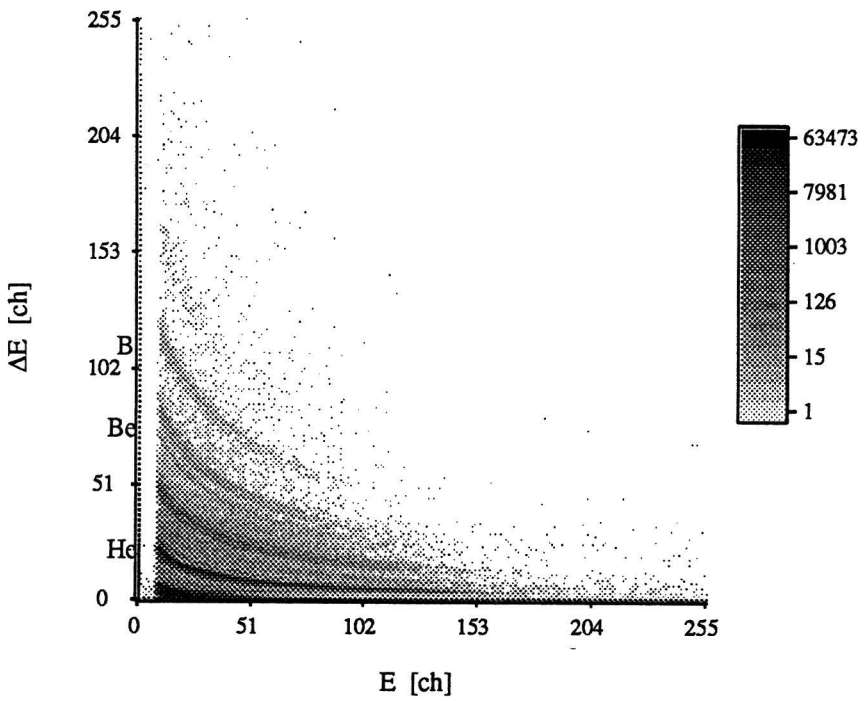

Figure 5.3: *ΔE-E plot of the measurement done to look at the light output relation.*

The analysis was done in several steps. The first step was to get the curves of the different ions in the plot as numerical values. Therefore all plots were divided in 'vertical' slices of one or several channels thick. This gives histograms and manually could be indicated which peaks in the slices were caused by which kinds of ion. A gaussian function was fitted with a least squares fit over parts of the slices. All software for this analysis was written in Pascal. The function has the form:

$$f(x) = \beta_3 e^{-(x-\beta_1)^2/\beta_2} \tag{5.1}$$

Then, β_1 gives the center of the curve. This is assumed to be the vertical value (energy of the ΔE detector) that corresponds to the horizontal value (energy of the GSO). The accuracy of this parameter is given by the semi-empirical formula:

$$\delta\beta_1 = \sqrt{\frac{(\pi\beta_2^3)^{\frac{1}{2}}}{(\beta_3^2\pi\beta_2)^{\frac{1}{2}} - 3}} \cdot \frac{1}{2\ln(2\beta_2)e^1} \tag{5.2}$$

The number of counts can be obtained by the area under the gaussian curve:

$$\int_{-\infty}^{\infty} dx\, f(x) = \beta_3\sqrt{\pi\beta_2} \tag{5.3}$$

A schematic view of this procedure is given in figure 5.4.

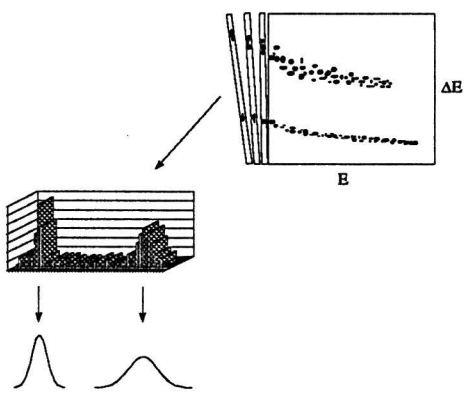

Figure 5.4: *Schematic view of the first steps in the analyzing of the data of the GSO telescope.*

The result is given in the following energy-light output graphs for all the ions up to ^{12}C.

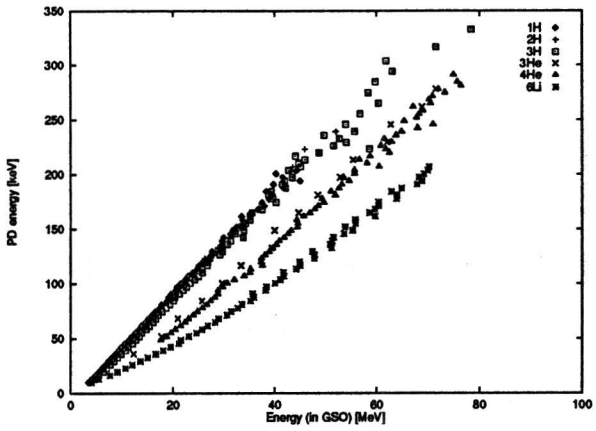

Figure 5.5: *Light output in GSO for various ions.*

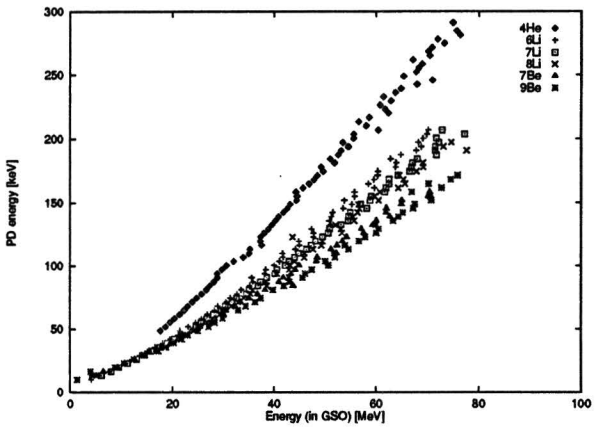

Figure 5.6: *Light output in GSO for various ions.*

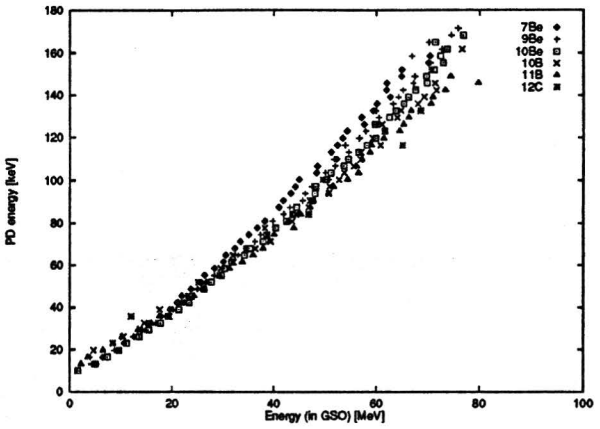

Figure 5.7: *Light output in GSO for various ions.*

Collimator

The use of a collimator in this experiment is to prevent particles from leaving the crystal at the side without transferring all of its energy to the crystal. This will mostly happen with particles with high energies. Therefore this effect will be visible as less particles with high energies (and relatively more particles with lower energies). Therefore it is very useful to look at the number of particles per energy interval. This is done for protons, deuterons, tritons and alpha's. Since the measurements with and without collimator are two different measurements, the number of counts has to be normalized. The plots are shown in figure 5.8.

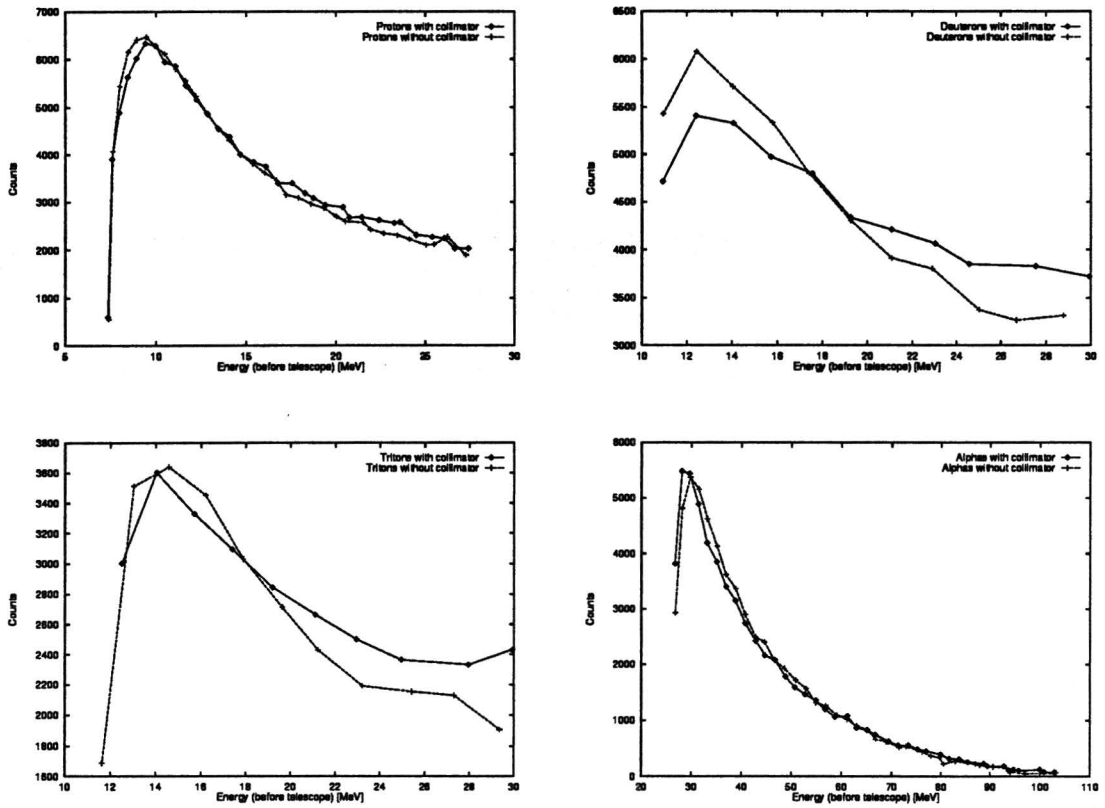

Figure 5.8: *The difference for the number of protons, deuterons, tritons and alpha's per energy interval for a GSO telescope with and without collimator.*

Monte Carlo simulations

Several Monte Carlo simulations were performed by Vladimir Avdeichikov, to simulate the effect of the collimator. The results are shown in appendix I in the form of a graph. In his simulations protons were used which were uniformly distributed in a energy range between 0 and 80 MeV. This resulted in an output spectrum that has relatively more low energy particles than high energy ones. It is possible to fit this spectrum with a straight line. The slope of this line is $-5 \cdot 10^{-3}$ MeV^{-1}.

By dividing the values with and without collimator in figure 5.1.2, a normalization is performed, that creates a virtually uniform distribution in energy of the particles. A straight line can be fitted through these points. A plot of the points and the fitted line is given in figure 5.10.

It is not possible to directly compare the slope of the line in this plot with the Monte Carlo simulation in appendix H. That is because the slope is dependent on the energy interval that is observed. This determines the scaling and therefore modifies the slope. An example is shown in figure 5.9. The normalization is done by equalizing the number of counts under the curve. For the interval $[a{:}b_1]$, the numbers under the straight line is given by: $b_1 - a$. The line l can be described by

$$l(E) = \alpha E + \beta \tag{5.4}$$

number under the line $\alpha E + \beta$ is given by

$$\int_{a}^{b_1} (\alpha E + \beta) dE \tag{5.5}$$

When a normalization on a interval $[a{:}b_2]$is performed, the new line is given by

$$h(E) = C \cdot l(E) = C\alpha E + C\beta \tag{5.6}$$

Since the integral should by equal with $b_2 - a$, C can be calculated by:

$$C = \frac{\frac{1}{2}\alpha(a_1 + b_1) + \beta}{\frac{1}{2}\alpha(a_2 + b_2) + \beta} \tag{5.7}$$

This means that the slope of the line at an observed interval $[a_1{:}b_1]$should be multiplied with C to get the value of the slope for an observed interval $[a_2{:}b_2]$.

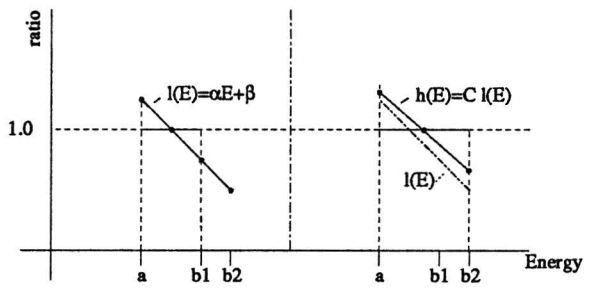

Figure 5.9: *Visualization of the change in slope when the normalization is changed*

The slope for the measured protons in figure 5.1.2 is $-5.68 \cdot 10^{-3}$ MeV^{-1}. This is 14 % larger than the value in the Monte Carlo simulation.

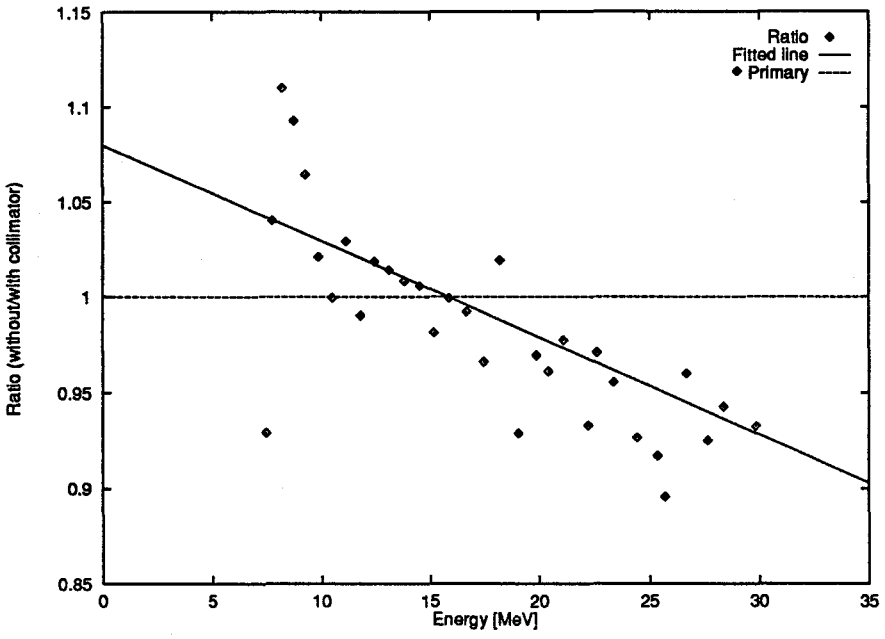

Figure 5.10: *Ratio between number of particles for the GSO detector with and without collimator for different energy intervals.*

Light output relation

A scintillation crystal has, contrary to a silicon detector, a very non linear energy response. Not only is the output non linear in respect to the energy of the incoming particle, but also the energy response is different for different kinds of ions. Formula 2.25 gives the light output function. This formula shows that there are three (actually two; a_0 is just an offset that will be observed in a experiment) parameters that define the response of the crystal. These parameters can be derived from the ΔE-E plots. Therefore you need finally for the different ions the energy of the incoming particles and the corresponding energy produced by the crystal. Since the particles have passed the silicon detector, the initial energy (the energy of the particle before passing the detector) can be calculated from the energy loss in the detector. And then also the rest energy is known. For calculating the energy loss in the detector, formula 2.6 is used.

In [AVD94] the quenching effect is defined as the ratio of light output between an incoming proton and ^{3}He at 30 MeV. It turned out that within the accuracy of the calibration, the quenching can vary between 0.56 and 0.65. Since exactly the same crystal and photo diode was used for the measurement that is described in [AVD94], a calibration is chosen that gives the same quenching effect as in that measurement (0.60).

Another thing that can be very important is the pulse height defect (PHD). The signal produced by heavier ions in the ΔE detector will be a little smaller as compared with the signal of a proton with the same energy. Formula 2.17 gives a estimation for this effect. Furthermore, it turns out that for the energy range and the ions we have used that

$$\frac{dE_{GSO}}{dE_{\Delta E}} < 0 \tag{5.8}$$

This means that when the real energy of the particle is higher than the measured energy in the ΔE detector then the particle has a lower energy in the GSO crystal than expected. Taking the value 20 for the detector dependent factor A in equation 2.17 (this is an average value for low resitance

surface barrier detectors), the error in the energy is less than 1 % for ^{10}B. Applying equation 5.2, the data for ^{10}B is around 3.5 % (0.1 % for protons). So the pulse height defect can be neglected.

Figure 5.5 to 5.7 shows the light output for the all different ions up to ^{12}C in the GSO crystal. By fitting the light output formula (equation 2.25) with the measured points, one get the three parameters. This fitting is done with a least square fit. I have rewritten and improved a fitting routine out of the NAG series. This is described in appendix E. The result of the fit was:

parameter	value
a_0	-3.5 keV
a_1	4.815 keV/MeV
a_2	0.8154 keV/(amu e^2)

5.2 Conclusions

The GSO crystal gives in combination with the photo-diode readout full isotope separation. The light output is determined and the Monte Carlo simulations done for the ion trajectories in the crystal are in 20 % consistence. It is not possible to use normal timing electronics for triggering with the GSO-photo diode detector.

Chapter 6

Pulse shape analysis

As explained in chapter 2.2.2, the shape of the pulse that comes from a detector gives information about the ion that has caused the pulse. Recently, the group of Pausch [PAU95] has done successful measurements to get mass separation by using pulse shape analysis (PSA) on fully depleted reversed (irradiated from the backside) silicon detectors. This has inspired us to look whether this is a good alternative for the ΔE-E telescope. They showed that the mass separation gets better for particles with higher energies. So an important parameter to look for is the lowest energy where the mass separation is still possible. Since the pulse shape effect is larger when the particles enter the detector from the back-side, we have reversed all detectors in the tests described below.

Also a scintillator crystal gives different shapes of its light output pulse for different ions. We have tried to observe this effect with the GSO-crystal - photo diode combination.

6.1 CELSIUS

The first measurements we have done with pulse shape analysis, were with the two Intertechnique detectors in the CELSIUS ring (see 3.1.4). The used reaction was ^{40}Ar on a ^{20}Ne gas target. Figure 6.1 shows the ΔE-E plot of the observed particles. The curves are due to protons, deuterons and tritons. Although these particles were not resolved in Pausch's measurements, it was a good opportunity to test our electronical set-up.

The PSA works only when a particle is fully stopped in a detector. Therefore, we used the first detector in the telescope for the PSA and the second detector to detect whether a particle is stopped. In figure 6.1, the result of the measurement is shown where the last detector was used to exclude the particles that were not stopped. But since the telescope did not have a common collimator, it is not sure that all particles were in anti-coincidence. Therefore another measurement is done where only the events are shown which were in coincidence with the second detector. This is shown in figure 6.1. This shows that the horizontal line is caused by particles that were not stopped. The important parameters that could be changed in our measurement was the time constant of the amplifier and the 'beta factors' (is a measure for the fraction) of the constant fraction discriminator. The best time constant was 0.25 μs. This was also the lowest time constant available. We know from the theory that a time constant around 100 ns is optimal. For the starting and stopping of the TAC, the best result was a beta factor of 0.1 and 0.5. Only this measurement is shown at in figure 6.1.

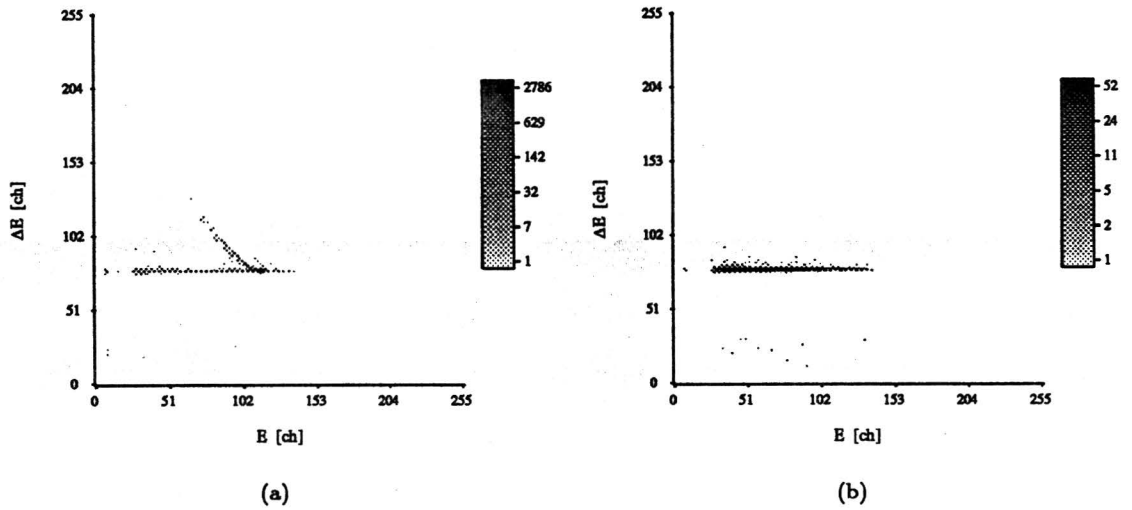

Figure 6.1: *The pulse shape of hydrogen isotopes measured in anticoincidence (a) and coincidence (b) with particles that are not completely stopped in the detector.*

6.2 Gamma cave

Several detectors were tested during the gamma cave test in cooperation with the group of Pausch. The used reaction and produced reaction products are already described in chapter 4. We have tested the following detectors:

Manufacturer	area	collimator	thickness	Project
Intertechnique	600 mm^2	ø15 mm	300 μm	-
Micron	50 x 50 mm	ø15 mm	300 μm	ISIS ([DAN94])
Micron	10 x 10 mm	-	1000 μm	-
Intertechnique (custom)	750 mm^2	-	500 μm	EUROBALL ([GRA94])

A promised Canberra PIPS detector could not been tested due to late delivery.

For all these measurements, the electronics of M. Moszynski were used. The important parameters that could be changed were the bias voltage and the beta factor in the constant fraction discriminator. It is not useful to display all measurements. In figure 6.2 an example is given for one of the best measurements. An isotope separation can be observed for ^{7}Be and ^{9,10}Be.

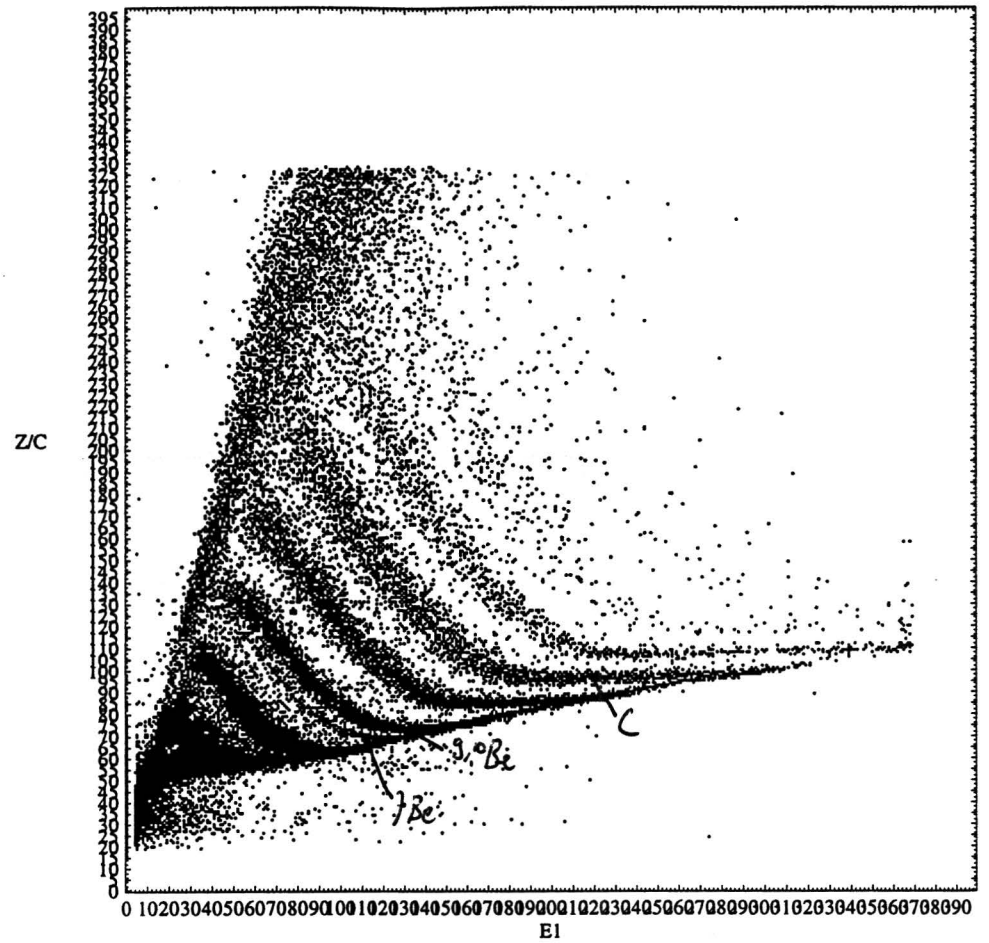

Figure 6.2: *Pulse shape analysis with a custom made Intertechnique detector.*

The important conclusions from the measurements were:

- An optimal 'pulse shape resolution' is obtained when the bias voltage is around the voltage where the detector is fully depleted.
- The best energy resolution is obtained when the bias voltage is much higher than the depletion voltage (reversed detector).

This means that an optimum has to be found for the bias voltage.

- The custom made Micron detector could get the lowest energy where mass separation was possible. This values lay around 2 A MeV for alpha's.

Two important characteristics for a detector that will be used for pulse shape analysis are [CHM95]:

- A good resistivity uniformity. A practical value will be a deviation of not more than 5 %.
- A high internal field which should be at least 0.3 V/μm.

Taking these characteristics into account, a new p-type detector should be ideal for PSA. The internal field for a p-type detector is higher (with the same resistivity and applied voltage) than a n-type detector. Also, the way a p-type detector is produced can guarantee a deviation in uniformity that is less than 3% [AVD95]. But the problem with a p-type detector is the fact that the plasma erosion and drift time (see 2.2.2) works in a opposite direction on the pulse shape. This can give difficulties like crossing particle curves in the plots or even no pulse shape information at all. The group of Pausch is making simulations to find out whether a p-type detector can be built that does not have these problems in the energy and ion range we are going to use.

6.3 Canberra PIPS detector

Canberra has lent us a 500 μm 'Passivated Implanted Planar Silicon' (PIPS) detector that is specially designed for pulse shape analysis. To test the PIPS detector for the uniformity in resistivity I used the small detector chamber with a ^{226}Ra source. The method is not directly straightforward and needs some explanation.

As mentioned in chapter 2.2, the depletion depth of a silicon detector is proportional to the square root of the resistivity and the voltage. In figure 6.3 a non fully depleted reversed detector is drawn. When a particle impacts on the detector it has to cross a certain thickness of silicon that does not act as a detector but only is an absorber. It has to be mentioned that the border between 'depleted' and 'non depleted' is in a real detector not as sharp as drawn.

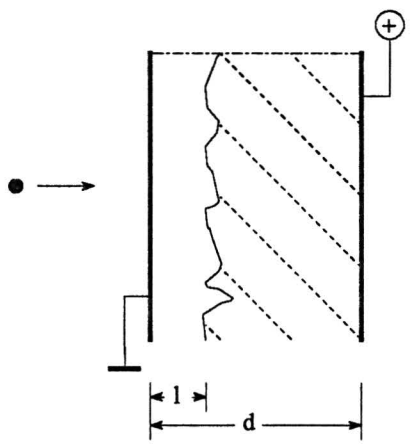

Figure 6.3: *Cross section of a non fully depleted detector. (hashed part is depleted)*

The thickness of the absorber in figure 6.3 is given for $V < V_{dep}$, using equation 2.16, by:

$$l = d - a\sqrt{\rho V} \tag{6.1}$$

So the measured energy E_m depends on the real particle energy:

$$E_m = E - \frac{dE}{dx}(E) \tag{6.2}$$

When $dE/dx(E)$ is supposed to be constant (or at least does not vary much compared to the other variables) over the used interval, then the channel number corresponding to the measured energy would be given by:

$$ch = b_1\sqrt{\rho V} + b_2 \tag{6.3}$$

Here in, b_1 and b_2 are two parameters that depend on the calibration and the characteristics of the detector. This gives directly the correlation:

$$\rho V = (\frac{ch - b_2}{b_1})^2 \tag{6.4}$$

The Canberra PIPS detector has a thickness of 500 μm and is specially designed to work with particles entering from the backside. The recommended bias voltage is 140 V with a leakage

current of 67 nA. It can be seen (this will be later explained for figure 6.6) that the detector is already fully depleted at 110 V. A measured ^{226}Ra spectrum with a bias voltage of 148 V and a current of 66 nA looks like figure 6.4.

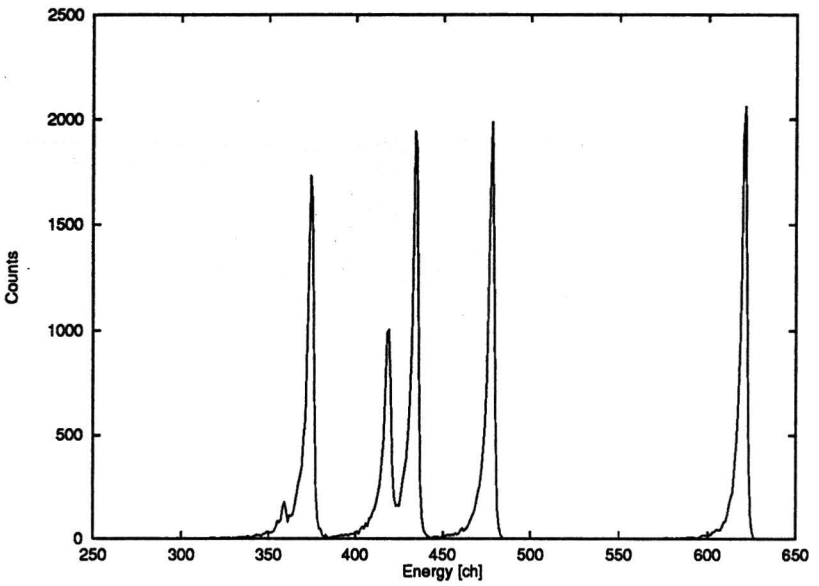

Figure 6.4: *^{226}Ra spectrum with 148 V bias.*

The same spectrum for a bias voltage of 75 V looks like figure 6.5. Not only are the positions of the peaks moving, but also the resolution decreases enormously.

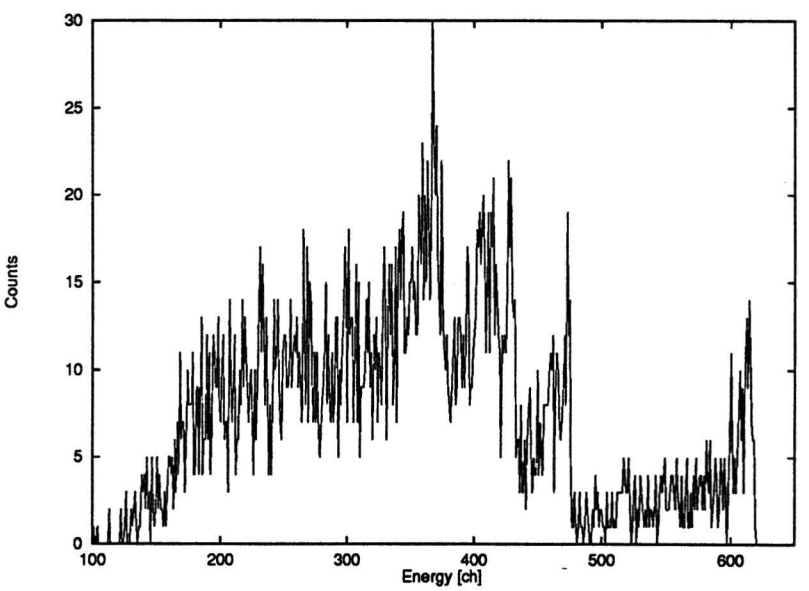

Figure 6.5: *^{226}Ra spectrum with 75 V bias.*

A plot for peak position (points) and equation (6.3) (line) with the correct parameters is given in

figure 6.6. It is clear that equation 6.3 only is valid for $V < V_{dep}$.

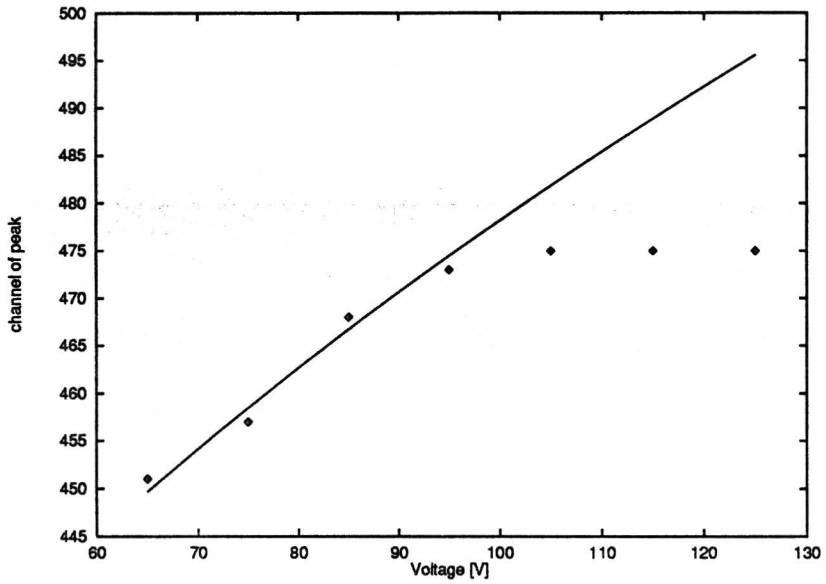

Figure 6.6: *The channel of the peak versus different bias voltages. The points give the measured values and the line the equation.*

The measured values for a line scan of ρV are shown in figure 6.7.

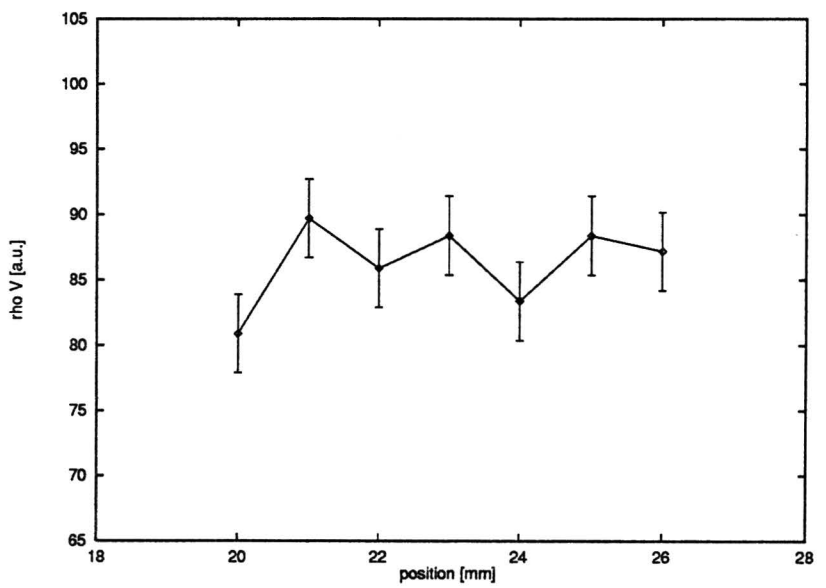

Figure 6.7: *ρV versus position plot.*

The result of the measurement of the 300 μm Micron detector that was used in the gamma cave is shown in figure 6.8.

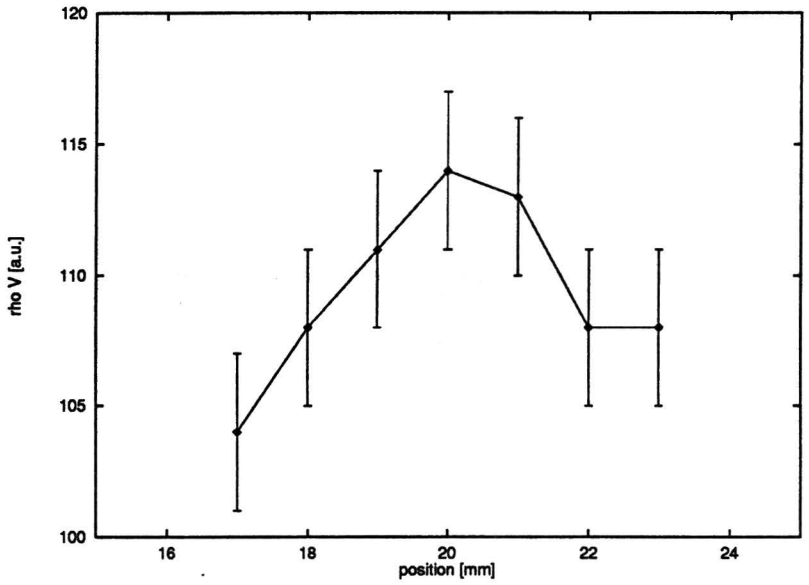

Figure 6.8: *ρV versus position plot.*

6.4 Pulse shape with GSO

The pulse shape of a scintillator crystal gives like a silicon detector information about the kind of ion. We have looked at this pulse shape although V. Avdeichikov had calculated that with the used cesium concentration in the crystal the time constants did not match the speed of the photo diode. The used electronics to get a ΔE-E plot are given in chapter 3.2.2. The energy slice, that was used for the measurement, is given in figure 6.9 as the bold plotted events. The result of the PSA is given in figure 6.10 that shows on the vertical axis the ΔE value which corresponds directly to a certain ion. On the horizontal axis the pulse shape is given. You can directly see from figure 6.10 that there is no difference in pulse shape for hydrogen and helium ions.

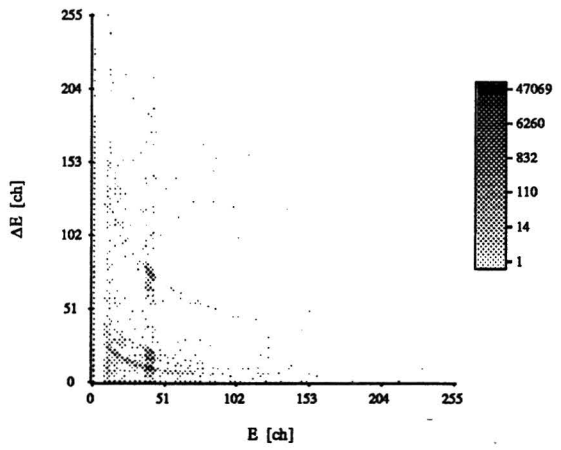

Figure 6.9: *ΔE-E plot for the used reaction. The bold events are the events that are selected by the single channel analyzer.*

simulations to obtain their performances. This is described in chapter 7.5. In 7.4 is discussed which requirements determine the performance of a time detector. To understand the concept of the time detector, it is useful to look somewhat deeper in the production of secondary electrons and the working principles of Multi Channel Plates. This is described in the next two sections.

7.1 Secondary electrons

When an ion passes matter, it will free electrons from this matter. There are several processes ([WHIPC]) that frees this electrons. Although in [SEI67] the name 'secondary electrons' only is used for one type of process, one normally use this name for all electrons that are produced.

The two main processes that contribute to the production of secondary electrons are elastic and inelastic reflection and Auger electrons. The reflected electrons have a velocity distribution around the direction of the ion. Most electrons have a low energy around 5 eV. The probability for producing electrons decreases for higher energies. The Auger electrons have some well defined energies but have a random direction. But since the Auger electrons are produced inside the matter, the distance that the electrons have to travel through the matter to reach the surface has too be taken into account. Therefore one will also observe a forward directed distribution for the Auger electrons. Figure 7.1 shows the energy spectrum and simplified velocity distribution.

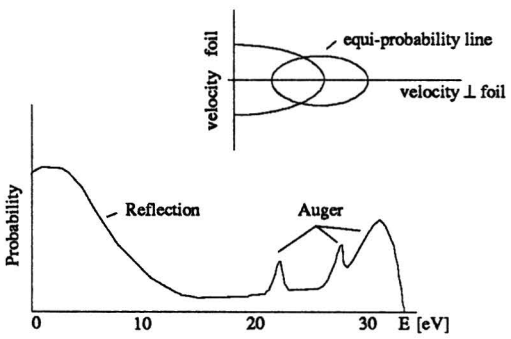

Figure 7.1: *Energy and space distribution of the secondary electrons produced by an ion that passes a foil.*

7.2 Multi Channel Plates

A Multi Channel Plate (MCP) is a secondary electron multiplier consisting of an array of millions of glass capillaries (channels) having an internal diameter ranging from 10 to 20 μm fused into the form of a thin disk less than 1 mm thick. The inside wall of each channel is coated with a secondary electron emissive material having proper resistance, and both ends of the channels are covered with metal thin films which acts as electrodes, thus each channel becomes an independent secondary electron multiplier. Figure 7.2 shows a drawing of a MCP.

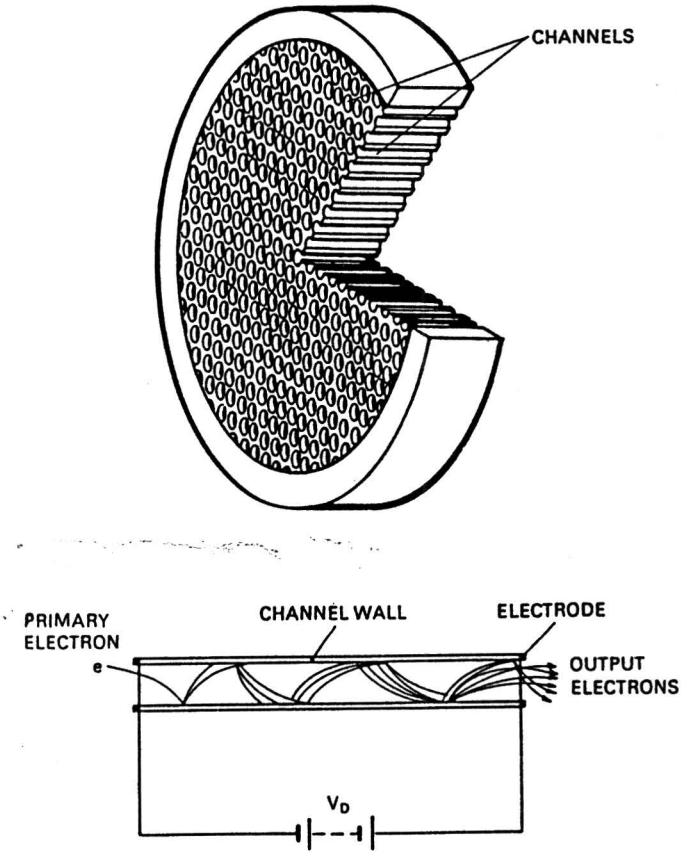

Figure 7.2: *Simplified drawing of a Multi Channel Plate and how it works.*

The channels have in generally an angle with the surface, called the bias angle. This bias angle lays between 5^o and 13^o and makes sure that an electron is hitting the wall of the channel. Since MCP's in time detectors are mostly used in pairs, the detectors are placed in such a way that the bias angles are opposite in both MCP's. This prevent ions traveling through the channels. This ion feedback is the limiting factor for the maximal amplification of a MCP. The amplification depends on the applied voltage and is mostly adjusted to 10^4 times. Once a channel has amplified the incoming electron, it needs time to recharge itself. This causes a deadtime that lays between 10 and 100 μs. Another imperfection can be seen in figure 7.2. The surface consists not only of the channels, but there is also inactive surface material. Normally, 40 % of the incoming electrons will not hit a channel and are simply lost.

7.3 Concept

The main concept of many time detectors is based on the fact that when an ion passes a foil, it produces secondary ions. This process is described in section 7.1. These electrons can be accelerated towards a MCP that can amplify the current. This pulse can be used as time signal.

Figure 7.3 gives a schematic view of how this concept is implemented in the the St.Petersburg detector. An ion can pass a foil and proceeds on its way through the hole in the MCP. The thin foil is made of 5-10 $\mu g/cm^2$ Al_2O_3 and is used to generate the secondary electrons. This foil is kept on a electric potential around -1000 V. Since Al_2O_3 is an electrical insulator, a thin layer of gold is evaporated on this foil to make it possible to supply the electrons on the entire foil. A ring on ground potential is used to accelerate the electrons and to defocus them, so they will not disappear through the hole in the MCP. The ring is in reality for this detector a square of four wires with a diameter of 50 μm. The electrons will hit the MCP and generate a current pulse that

can be used for starting or stopping a timer. The front face of the MCP has a potential around -600 V. The dimensions are given in the figure.

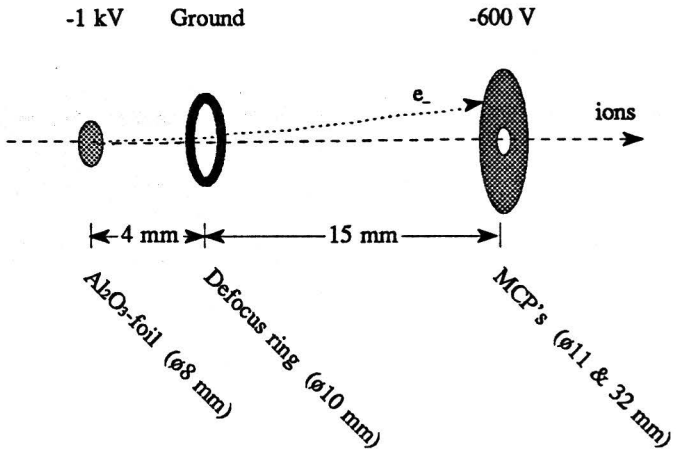

Figure 7.3: *Concept of the St. Petersburg detector.*

7.4 Requirements

The performance of a time detector depends on several things. The most important ones are the global time resolution, the local time resolution and the efficiency.

Global time resolution

Most effort during the design of a time detector is mostly put into the optimalization of the global time resolution.[2ex] The ions can pass the foil somewhere on its entire area. This will release secondary ions on the spot where the ion has passed. Due to geometrical effects and the shape of the electric field, the time that the electrons need for reaching the MCP (drift time) will differ for different places on the foil. Since one does not have any information about the place where the ion has passed, this difference in drift time is just an uncertainty and this directly contributes to the total time resolution.

Local time resolution

The drift time as described in previous section, is not only determined by the place on the foil, where the secondary electrons are produced. When an ion passes a foil on a certain place, it will produce secondary electrons with a distribution in energy and emitting angle. This will give different paths for the electrons and therefore different drift times. I will call this the local time resolution.

The difference between global and local time resolution manifest during an experiment. Looking on an oscilloscope at the pulse, one observes the local time resolution. But when the detector is used in a mass spectrum telescope, the total time resolution will determine the mass resolution.

In the rest of this chapter, the *time resolution* is the combination between local and global time resolution.

Chapter 7

St.Petersburg Time detector

For detecting low energy particles (< 0.7 A MeV) with the CHICSi telescope, one cannot use silicon ΔE-E telescope because the thin first detector will stop these particles. Therefore, there is a concept to use time of flight-energy (ToF-E) telescopes for this purpose. A ToF-E telescope works with two time detectors and an energy detector. The velocity of the particle is measured by the time that the ion needs to travel between the two time detectors. By measuring the energy, one can calculate the mass of the particle.

In [WHI91] is shown how the time resolution of the time detector and the energy resolution in the energy detector affects the mass resolution of the whole telescope. One can derive what the time resolution has to be to have the same influence on the mass resolution as the energy resolution of the energy detector has. When the energy of the ion E is given in MeV, the mass M in amu, the distance between the time detectors L in meters and the energy resolution δE in MeV, then the time resolution δT is given in seconds by

$$\delta T = \sqrt{1.30 \cdot 10^{-15} \frac{ML^2}{E^3} \delta E^2} \tag{7.1}$$

Taking as distance of 15 cm and an energy resolution of 20 keV (should be even lower since we are using PiN diodes as energy detector), next table shows the needed time resolutions of the time detector (δM_E and δM_T are the influences of the energy and time resolutions on the mass resolution).

Particle	Energy	Time resolution for $\delta M_E = \delta M_T$	Time resolution for δM_T=0.5
p	0.05 MeV	9.66 ns	6.05 ns
p	0.7 MeV	184 ps	1.62 ns
^{12}C	0.05 A MeV	81 ps	505 ps
^{12}C	0.7 A MeV	15 ps	135 ps
^{40}Ar	0.05 A MeV	24 ps	151 ps
^{40}Ar	0.7 A MeV	4.6 ps	40 ps

With the present time detectors (with time resolutions around 200 ps), it is clear that most effort in designing ToF-E telescopes should be put in the time detectors.

In [WHI91], a time detector inspired by the Busch mirror detector is tested. Simulations to obtain the time resolution are described in [WRI90]. Also a other kind of time detector is described in [BAT95]. This detector is used for neutron spectrometry and is supposed to give a time resolution around 80 ps, but it is not completely understood why it can give this performance. The concept of this detector is given in 7.3. Although the detector cannot be used in this geometrical form, it is very interesting to find out how it performs, so one can use these principles in future time detectors. To compare these two time detectors without building them, one can use computer

simulations to obtain their performances. This is described in chapter 7.5. In 7.4 is discussed which requirements determine the performance of a time detector. To understand the concept of the time detector, it is useful to look somewhat deeper in the production of secondary electrons and the working principles of Multi Channel Plates. This is described in the next two sections.

7.1 Secondary electrons

When an ion passes matter, it will free electrons from this matter. There are several processes ([WHIPC]) that frees this electrons. Although in [SEI67] the name 'secondary electrons' only is used for one type of process, one normally use this name for all electrons that are produced.

The two main processes that contribute to the production of secondary electrons are elastic and inelastic reflection and Auger electrons. The reflected electrons have a velocity distribution around the direction of the ion. Most electrons have a low energy around 5 eV. The probability for producing electrons decreases for higher energies. The Auger electrons have some well defined energies but have a random direction. But since the Auger electrons are produced inside the matter, the distance that the electrons have to travel through the matter to reach the surface has too be taken into account. Therefore one will also observe a forward directed distribution for the Auger electrons. Figure 7.1 shows the energy spectrum and simplified velocity distribution.

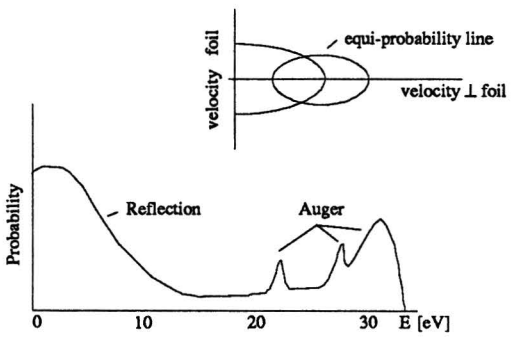

Figure 7.1: *Energy and space distribution of the secondary electrons produced by an ion that passes a foil.*

7.2 Multi Channel Plates

A Multi Channel Plate (MCP) is a secondary electron multiplier consisting of an array of millions of glass capillaries (channels) having an internal diameter ranging from 10 to 20 μm fused into the form of a thin disk less than 1 mm thick. The inside wall of each channel is coated with a secondary electron emissive material having proper resistance, and both ends of the channels are covered with metal thin films which acts as electrodes, thus each channel becomes an independent secondary electron multiplier. Figure 7.2 shows a drawing of a MCP.

Efficiency

The number of secondary electrons (with the foils normally used for time detectors) is around 100 per passed ion. Even when they all reach the MCP, not all of them will contribute to the final signal.

A MCP can only amplify (due to its structure) 60 % of the incoming electrons. Also, it cannot amplify all electrons that fall in the same area (due to the dead time of a channel). So one has to be careful not to lose to many electrons during there drift, otherwise only a few electrons determine the final signal, and this cannot be distinguished from the noise produced by lose electrons.

7.5 Simulation

For the simulation ([JOH92]) of the electron trajectories, I have used the FORTRAN SLAC routines, originally written in the beginning of the 70's at the Stanford University and the Royal Institute of Technology in Stockholm ([NIL73]) for use on an IBM 360 main frame and later converted to VMS systems. It is a powerful program that can be adjusted for many physical influences. It was also used for designing the electron gun for the 300 keV electron cooler of the CELSIUS ring.

The program can solve both cartesian and rotational symmetrical problems. As boundaries one can use insulators, conductors on a certain potential or grids. Not only electrical fields can be applied. Also external magnetic fields can be taken into account. The program can also calculate the electric field caused by the space charge of the electrons and the magnetic field induced by the movement of the charge.

I have converted the program to the VMS APX ('DEC Alpha') and adjusted it to fulfil our needs and also rewritten the graphical output conversion so that it directly delivers Postscript output.

For the initial velocities of the electrons, I have used 1000 randomly generated velocities, with a distribution that looks like the velocity distribution described in section 7.2. An example of these generated velocities is given in a plot in figure 7.4.

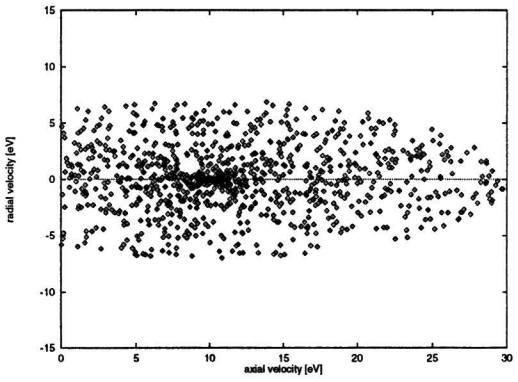

Figure 7.4: *The velocity distribution for 1000 secondary electrons.*

7.6 Result

In figure 7.5, a (rotational) cross section of the detector is shown. The boundary consists of the foil, the ring and the MCP. Also the equi-potential lines and the trajectories of twenty electrons are visible.

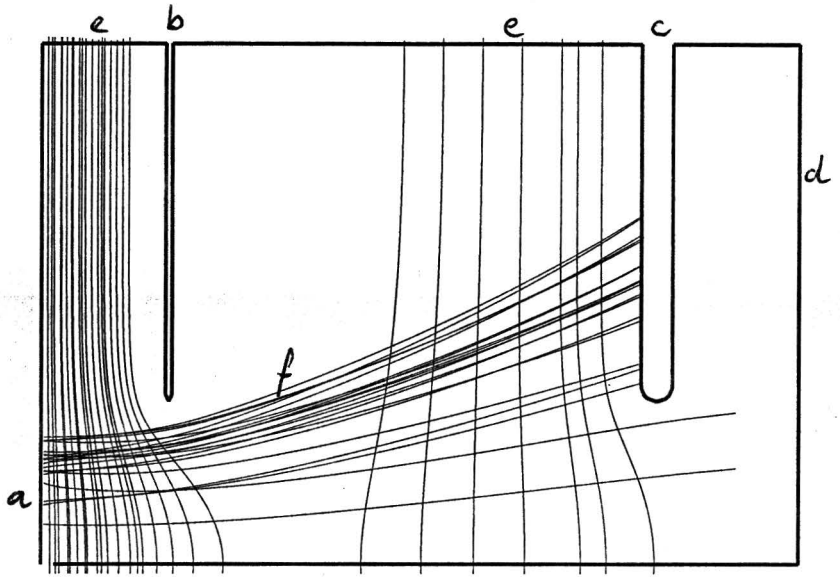

Figure 7.5: *Rotational cross section of the result of a simulation. a) Foil b) Ring c) MCP's d) Boundary e) equi-potential lines f) electron trajectories*

This kind of simulation is done with 1000 electrons, each time emitted from a different point on the foil, to look at the local time resolution. This is done for a radius of 0.25, 0.75, 1.25 ... 3.75 mm. Assuming that in reality the ions impact on the foil equally distributed over the whole surface, then this means that there will be relatively more incoming particles around the larger radii than at the smaller ones. This is because one has to look at the area that the radius represent. In the following table, the areas are given.

Min radius	Max. radius	Radius in Simulation	Area [cm^2]	Part [%]
0.0	0.5	0.25	0.78	1.6
0.5	1.0	0.75	2.36	4.7
1.0	1.5	1.25	3.92	7.8
1.5	2.0	1.75	5.50	10.9
2.0	2.5	2.25	7.07	14.1
2.5	3.0	2.75	8.64	17.2
3.0	3.5	3.75	10.2	20.3
3.5	4.0	3.75	11.8	23.4

This indicates that it is more important to look what happens with the electrons that are emitted from the outer part of the foil, than the ones that are produced in the center.

A result of the simulation is given in the form of a histogram in figure 7.6. The drift time in this figure is the time that the electrons needed to travel from the foil to the MCP.

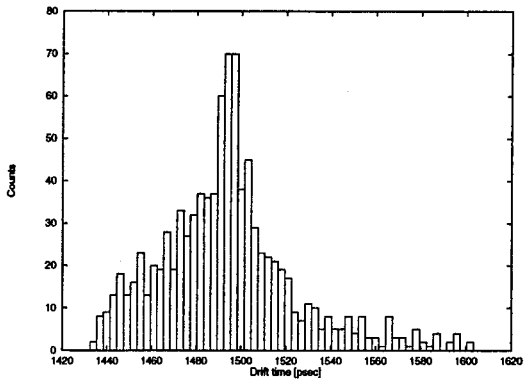

Figure 7.6: *Histogram of the drift time for the produced electrons.*

By counting the number of electrons that finally hit the MCP, one knows directly the efficiency. For the average drift time and the time resolution, a gaussian function is fitted with a least square fit over the histograms. The center of the curve represents the average time and the FWHM (full width half maximum) gives the time resolution. The results are shown in figure 7.7, 7.8 and 7.9.

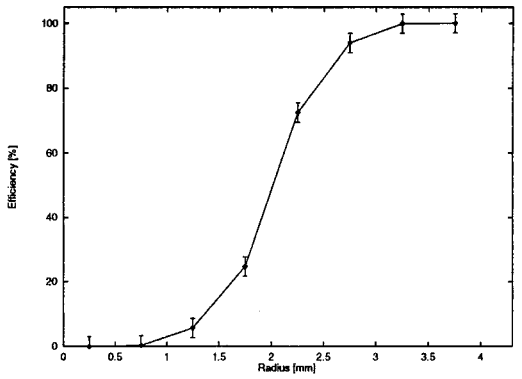

Figure 7.7: *Efficiency of the detector for different radii on the foil*

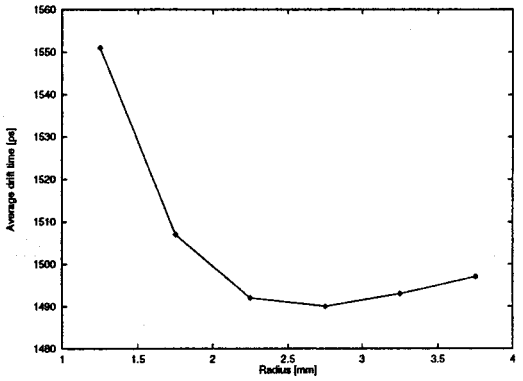

Figure 7.8: *The average drift time of the electrons in the detector for different radii on the foil*

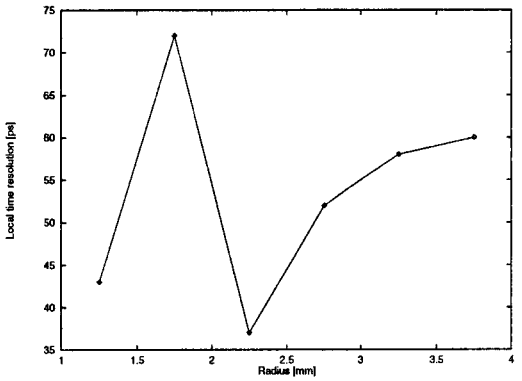

Figure 7.9: *The time resolution for different radii on the foil*

To look at the total time resolution, another simulation is done. In that case electrons were generated over the entire foil with a distribution that represents the surface distribution ($P(r) = \frac{3}{16}r^2$). The histogram of the drift times is given in figure 7.10. The efficiency is 71.1 %, the average drift time is 1498 ps and the time resolution is 60 ps.

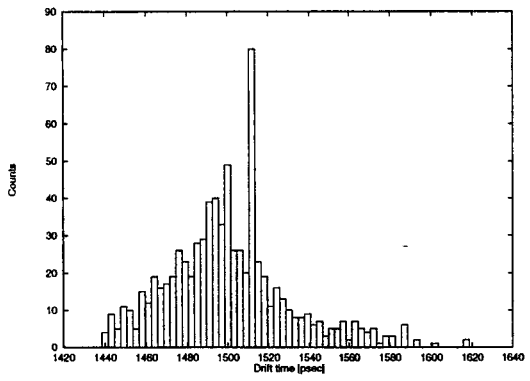

Figure 7.10: *Histogram of the local drift time for the produced electrons.*

7.7 Optimizing the detector

It is in humans nature to try to make things better. But history shows that not everybody thinks the same about what is 'better'.

The same problem arises when (during optimizing this detector) one has to decide whether a change is an improvement. In previous sections is shown that there are several ways to describe the performance. The two most important ones are the time resolution and the efficiency. So one has to find an optimal combination of those two values. But it depends on the kind of electronics and the background (of electrons) how important each value is. Therefore I will not optimize the detector, but just give the time resolution and the efficiency in several cases.

The main things that can be changed to optimize the detector are the distances between the different parts, and the applied voltages.

Optimizing using dimensions

I have made 9 different setups for the detector by changing the distances. Notice that setup 5 is the original design. The simulation is done with a distribution for the electrons over the entire foil. The same way of analysis as before is used to obtain the efficiency and time resolution. The result is shown in next table:

setup	Foil-ring mm	Ring-MCP mm	Efficiency %	Time resolution ps
1	3.0	13.5	72.6	57
2	4.0	13.5	68.3	57
3	5.0	13.5	64.0	60
4	3.0	15.5	75.3	60
5	4.0	15.5	71.9	59
6	5.0	15.5	67.1	62
7	3.0	17.5	77.9	68
8	4.0	17.5	74.3	61
9	5.0	17.5	69.4	63

Figure 7.11: *Different setups for the time detector.*

It is clear from this table that the efficiency get higher when the distance between the foil and ring gets smaller while the distance to the MCP get bigger. This can be explained by looking at figure 7.5. The loss of electrons through the hole is what causes a low efficiency. When the distance between the foil and ring is small, a stronger defocussing lens is created. By making a longer drift space towards the MCP, the electrons get longer the opportunity to drift radial and avoid the hole in the MCP. On the other hand, the time resolution gets better when all distances are small. This can be explained because all drift times gets smaller and therefore also the relative drift times. This gives a better resolution.

Another explanation can be given by looking at the initial velocities of the electrons. Only when the electrons have a low energy, the initial energies play an important role in the drift time. When the distance between the foil and the ring is smaller, a stronger electric field is present at the foil. This makes the electrons accelerate faster and therefor the electrons have a shorter time a low energy. This also increases the time resolution.

Unfortunately, in a real detector, one has to take care that the distance between the different parts with a high potential difference does not get to small. This can give an electrical break through (at the insulators or just a corona discharge).

Optimizing using the potentials

Different voltages are applied to the foil and MCP's to look what the difference it gives in the performance. It has to be mentioned that in reality one cannot change that easy the potential of the MCP's, because this has a direct influence on there performance.

The different set-ups that I have simulated are:

Foil [V]	MCP [V]	Efficiency [%]	Time resolution [ps]	Remark
-1000	-100	60.5	52	
-1000	-600	71.9	59	Original design
-1000	-900	78.7	204	
-2000	-200	61.5	27	
-2000	-1100	77.5	65	

It is clear to see that the time resolution and efficiency are oppositely affected by a change in the potentials.

7.8 Conclusion

It looks like the St. Peterburg detector is a well functioning time detector that only is insensitive for ions that are passing on a 15 % area in the middle of the foil. The time detector has (compared to other known time detectors) a good time resolution around 60 ps. This is comparable with the 80 ns that was measured with this time detector. The simulation gives probably a better resolution, because it does not have the real life problems like deviation in distances, misallignements and disturbing fields. The efficiency around 72 % is sufficient to guarantee a sharp signal.

It looks like the following properties makes this design function well:

- The detector is small, which makes short drift paths for the electrons, and therefore differences in drift paths give small time differences. Also the small distances create (for normal voltages) high electrical fields, that strongly force the electrons to take certain trajectories.
- The detector can (due to its construction) easily be screened to prevent lose electrons to cause a background. Therefore one can give up efficiency to gain a better time resolution.

The real detector was optimized during operation, and the simulations show that it is a good compromise, that hardly can be improved.

Some real tests should be done to determine whether a carbon or a gold coated Al_2O_3 foil gives better results when the time detector is placed in a ToF-E telescope (energy straggling in the foil compared to produced electrons).

A problem that will arise during the building of the detector, is that not many manufacturers are able to make a hole in a MCP.

The geometrical form of the detector makes it unfortunately impossible to directly use it for CHICSi. But the concept can certainly used for designing new time detectors.

Chapter 8

Conclusions

It can be said that the SINTEF detectors can (although normal pre-amplifiers are used) form a mass analyzing telescope with a mass resolution comparable with e.g. a telescope that consists of a high quality p-type thin detector and a commercial thick detectors. The mass resolution is good enough to obtain full mass separation for the observed ions (up to ^{40}Ar). Unfortunately, the detectors are not stable and can be seriously damaged by a low (10^6 ions/cm^2) ion dose. This damage is observed as a high raise in the leakage current, but the energy resolution is not affected. In general, one has to test what influence the RF-structure in a storage ring has on the noise level of the thin detectors and what the performance of the detectors are in ultra high vacuum.

The combination of a 300 μm silicon detector and a cesium doped GSO crystal with photo diode readout as ΔE-E telescope seems to give full isotope separation for (the observed) ions up to ^{12}C. Although an optical medium (that cannot be used in the ultra high vacuum of the CELSIUS ring) was used for the coupling between the crystal and the diode, a vacuum gap will still give a better mass resolution than required. The Monte Carlo simulations (done by V. Avdeichikov) for the effect of a collimator on the background noise seems to give results that are within 20 % accuracy with the measurements. So, this simulation can be used to for further optimizing of the GSO crystal. Due to the low efficiency of the GSO scintillation crystal, normal timing electronics will give a very high (10th of MeV's) threshold. Therefore, the timing electronics in the readout chip has to be changed.

The pulse shape analysis gives promising results for mass analyzing telescopes. But this technique is not developed enough for use in the CHICSi telescope. Further development has to be done to get mass separation for ions with energies below 2 A MeV. This can probably be done by changing the design of the silicon detectors.

The design of the St.Peterburg time detector can unfortunately not be used in it present form for the CHICSi telescope. But it is certainly worthwhile to try to convert the well chosen properties to a compact time detector.

The decision to use silicon ΔE-E telescopes in combination with GSO-crystals with photo diodes in the CHICSi telescope, is at this moment the best choice. It will need some further development, but the results of this research in the collaboration will also be for the benefit of many other detector development projects.

Bibliography

[AVD94] V.V Avdeichikov et al., Light output and energy resolution of CsI, YAG, GSO, BGO and LSO scintillators for light ions, NIM A 349 (1994) 216.

[AVD95] Personal communication with V.V. Adveidikov.

[BAT95] O. Batenkov et al., High precision neutron spectrometer for study of spontaneous and ion induced fission, will be published during 1995.

[BIR64] J.B. Birks, The theory and practice of scintillation counting, Oxford, 1964.

[BRA91] P.J.M. Brands, J. Jonker, M.B Keuzenkamp and M.J.A. de Voigt, Nuclear analysis techniques, 1991.

[CLI90] L. Cliche, S.E. Gujrathi and L.A. Hamel, Pulse height defects for ^{16}O, ^{35}Cl and ^{81}Br ions in silicon surface barrier detectors, NIM B 45 (1990) 270.

[DAN94] G. DeAngelis, Euroball LCP Det. Meeting slide report, 1994.

[DIJ94] P.W.L. van Dijk et al, Stopping powers for channeled helium ions in silcon using electron densities drom bandstructure calculations, NIM B 85 (1994) 551.

[GRA94] H. Grawe et al., Proposal for a 4π Silicon Ball for EUROBALL, 1994.

[GUT93] M. Guttormsen et al., CHICSi a proposal for a multi-detector ΔE-E particle telescope, Univ. of Oslo report series UiO/PHYS/93-01, 1993.

[HOR92] D. Horn et al, The mass dependence of CsI(Tl) scintillation response to heavy ions, NIM A 320 (1992) 273.

[JOH92] Claes Johnson, Numerical solution of partial differential equations by the finite element method, 1992.

[KAU73] S.B. Kaufman et al., A calibration procedure for the response of silicon surface-barrier detectors to heavy ions, NIM 115 (1974) 47.

[KRA88] K.S. Krane, Introductory Nuclear Physics, Wiley, 1988.

[LAV89] L. Laverane-Gosselin et al., On the use of thin ion implanted Si detectors in heavy ion experiments, NIM A 276 (1989) 210.

[LOV95] W. Loveland et al., The pulse height defect of heavy ions in silicon surface barrier detectors, this article will be published during 1995.

[MOR73] D.V. Morgan, Channeling; Theory, observation and applications, London Cop., 1973.

[NAG15] Nag fortran library mark 15 volume 4

[NIL73] B.H. Nilsson ans M. Sedlaček, SPCGUN, a computer program for computations of electron guns with space-charge, Internal report of the Dept. of Electron Physics of the Royal Institute of Technology in Stockholm, 1973.

[PAU94] G. Pausch et al, Particle identification in a wide dynamic range based on pulse-shape analysis with solid state detectors, NIM A 349 (1994) 281.

[PAU95] G. Pausch et al., Pulse-shape discrimination with planar Si detectors, slides of a presentation given during a CHICSi meeting at TSL Uppsala, February 1995.

[SEI67] H. Seiler, Einige aktuelle Probleme de Sekundärelektronenemission, Z. angew. Phys. Heft 3, 1967.

[WAY66] Nuclear data sheets section A, volume 2, 1966.

[WHI91] H.J. Whitlow, B. Jakobsson and L. Westerberg, Mass resolution of recoil fragment detector telescopes for 0.05-0.5 A MeV heavy recoiling fragments, NIM A 310 (1994) 636.

[STE71] E.P. Steinberg et al., Pulse height response characteristics for heavy ions in silicon surface-barrier detectors, NIM 99 (1971) 309.

[VAR84] Basic vacuum technology training workbook, , Varian Associates inc., 1984.

[WIL70] B.D. Wilkins et al., Pulse-height defects for heavy ions in a silicon surface-barrier detector, NIM 92 (1970) 381.

[WHIPC] Personal communication with H.J. Whitlow.

[WRI90] Paul Wright, Development of a recoil fragment detector for CELSIUS, thesis, 1990.

[ZIEGL] U. Littmark and J.F. Ziegler, Handbook of range distributions for energetic ions in all elements, volume 6, Pergamon Press.

Appendix A

General parameters for a range formula

The parameters listed below can be used in formula:

$$R = \frac{m}{z^2}(P_{(1,Z)}x^{P_{(2,Z)}} - P_{(3,Z)} - P_{(4,Z)}e^{P_{(5,Z)}x} - P_{(6,Z)}x^{P_{(7,Z)}x}) \tag{A.1}$$

with x given by

$$x = \frac{E}{m} \tag{A.2}$$

When the energies are given in MeV, then the range is in μm.

The parameters P are given in the next table.

Z	1	2	3	4	5	6	7
1	12.33600	1.76990	7.51450	6.83780	0.86530	0.51530	39.48200
2	12.32960	1.76990	8.63580	7.53110	1.20160	0.92840	32.52540
3	12.37570	1.76990	13.87660	12.39580	1.15890	1.29760	33.47170
4	12.34020	1.76990	22.39060	20.57090	1.00020	1.64290	35.79480
5	12.36970	1.76990	30.23760	28.00920	0.96450	2.05090	34.80790
6	12.42090	1.76990	38.83640	35.74490	0.85290	2.69430	30.20140
7	12.55160	1.76990	45.52440	41.69340	0.82050	3.61950	27.07500
8	12.84100	1.76990	52.93840	48.07440	0.80840	4.67430	24.83480
9	12.91690	1.76990	66.09530	59.86480	0.71260	6.09440	22.64880
10	13.17930	1.76990	80.09350	72.21790	0.64660	7.79070	20.84350
11	13.84710	1.76990	88.70590	80.04890	0.67210	8.68040	21.01080
12	14.15130	1.76990	100.78390	91.12280	0.66190	9.76800	20.98440
13	14.67090	1.76990	109.31340	98.79600	0.68540	10.77500	21.16770
14	15.07750	1.76990	120.62610	109.06450	0.68300	11.92860	21.02360
15	15.48240	1.76990	132.45590	119.83840	0.67720	13.12800	20.78580

Appendix B

Parameters for the range formula

I have obtained the following parameters by fitting data from the tables used by Ziegler by a least square fit with the formula:

$$R(E) = \exp\left(p_0 + p_1 \ln(E) + p_2 \ln^2(E)\right) \tag{B.1}$$

When the energy E is given in MeV, the range will be in μm.

Mass	Charge	p_0	p_1	p_2
1	1	2.796306654	1.583700479	0.025202958
2	1	2.442732375	1.498994070	0.034599035
3	1	2.324695333	1.422456178	0.041675340
3	2	1.346181344	1.213011905	0.068463454
4	2	1.160418558	1.214890219	0.066165581
6	3	0.634821735	1.003620196	0.084304030
7	3	0.824115122	0.930754758	0.085246273
8	3	1.063513816	0.717651827	0.116801098
7	4	0.407264488	0.833563373	0.100063313
9	4	1.021870764	0.563832690	0.120461668
10	4	0.643200826	0.662497894	0.114426275
10	5	0.526138012	0.558030802	0.122468256
11	5	0.489035154	0.608915548	0.109758198
12	6	0.308952208	0.560409979	0.110380146
13	6	0.480822324	0.458011205	0.122469051

Appendix C

Kinematics and reaction products for the tandem tests

44 MeV $^{16}O \rightarrow {}^{27}Al$

The 44 MeV ^{16}O on ^{27}Al process gives the following reactions, assuming a Coulomb barrier of 34.5 MeV. The data is taken from [WAY66] and formulas 2.13 and 2.12 are used.

Reaction	Q-value	Treshold [MeV]
$^{27}Al(^{16}O,^{4}He)^{39}K$	9.45	-
$^{27}Al(^{16}O,^{1}H)^{42}Ca$	9.32	-
$^{27}Al(^{16}O,^{12}C)^{31}P$	2.50	-
$^{27}Al(^{16}O,n)^{42}Sc$	2.10	-
$^{27}Al(^{16}O,^{2}H)^{41}Ca$	0.056	-
$^{27}Al(^{16}O,^{3}H)^{40}Ca$	-2.04	3.2
$^{27}Al(^{16}O,^{3}He)^{40}K$	-3.33	5.3
$^{27}Al(^{16}O,^{4}He\ n)^{38}K$	-3.64	5.8
$^{27}Al(^{16}O,^{6}Li)^{37}Ar$	-5.07	8.1

With formula 2.8 and 2.11 the following kinematics can be calculated:

Angle [^{o}]	Process	ion	Energy [MeV]	Pass 16μm Si
30	scattering	^{16}O	40.5	Yes
30	recoil	^{27}Al	30.8	No

44 MeV $^{16}O \rightarrow {}^{12}C$

The 44 MeV ^{16}O on ^{12}C process gives the following reactions, assuming a Coulomb barrier of 26.8 MeV. The data is taken from [WAY66] and formulas 2.13 and 2.12 are used.

Reaction	Q-value	Treshold [MeV]
$^{12}C(^{16}O,^{4}He)^{24}Mg$	6.77	-
$^{12}C(^{16}O,^{1}H)^{27}Al$	5.17	-
$^{12}C(^{16}O,n)^{27}Si$	-0.4	0.9
$^{12}C(^{16}O,^{2}H)^{26}Al$	-5.66	13.2
$^{12}C(^{16}O,^{3}He)^{25}Mg$	-6.5	15.2

With formula 2.8 and 2.11 the following kinematics can be calculated:

Angle [°]	Process	ion	Energy [MeV]	Pass 16μm Si
30	scattering	^{16}O	35.6	Yes
30	scattering	^{16}O	7.7	No
30	recoil	^{12}C	32.1	Yes

35 MeV ^{12}C → ^{27}Al

The 35 MeV ^{12}C on ^{27}Al process gives the following reactions, assuming a Coulomb barrier of 24.5 MeV. The data is taken from [WAY66] and formulas 2.13 and 2.12 are used.

Reaction	Q-value	Treshold [MeV]
^{27}Al(^{12}C,^{1}H)^{38}Ar	10.2	-
^{27}Al(^{12}C,^{4}He)^{35}Cl	9.4	-
^{27}Al(^{12}C,n)^{38}K	3.5	-
^{27}Al(^{12}C,^{2}H)^{37}Ar	0.62	-
^{27}Al(^{12}C,^{3}H)^{36}Ar	-1.9	2.7
^{27}Al(^{12}C,^{3}He)^{36}Cl	-2.6	3.8
^{27}Al(^{12}C,^{6}Li)^{33}S	-4.7	6.8
^{27}Al(^{12}C,^{7}Li)^{32}S	-6.1	8.8

With formula 2.8 and 2.11 the following kinematics can be calculated:

Angle [°]	Process	ion	Energy [MeV]	Pass 16μm Si
30	scattering	^{12}C	32.9	Yes
30	recoil	^{27}Al	22.4	No

35 MeV ^{12}C → ^{12}C

The 35 MeV ^{12}C on ^{12}C process gives the following reactions, assuming a Coulomb barrier of 18.1 MeV. The data is taken from [WAY66] and formulas 2.13 and 2.12 are used.

Reaction	Q-value	Treshold [MeV]
^{12}C(^{12}C,^{4}He)^{20}Ne	4.6	-
^{12}C(^{12}C,^{1}H)^{23}Na	2.2	-
^{12}C(^{12}C,n)^{23}Mg	-2.6	5.2
^{12}C(^{12}C,^{2}H)^{22}Na	-8.0	16.0

With formula 2.8 and 2.11 the following kinematics can be calculated:

Angle [°]	Process	ion	Energy [MeV]	Pass
30	scattering	^{12}C	31.0	Yes
30	recoil	^{12}C	26.3	Yes

50 MeV ^{19}F → ^{12}C

The 50 MeV ^{19}F on ^{12}C process gives the following reactions, assuming a Coulomb barrier of 20.5 MeV. The data is taken from [WAY66] and formulas 2.13 and 2.12 are used.

Reaction	Q-value	Treshold [MeV]
$^{12}C(^{19}F,^{1}H)^{38}Ar$	15.7	-
$^{12}C(^{19}F,^{4}He)^{27}Al$	13.3	-
$^{12}C(^{19}F,n)^{30}P$	10.0	-
$^{12}C(^{19}F,^{2}H)^{29}Si$	7.3	-
$^{12}C(^{19}F,^{3}H)^{28}Si$	5.1	-
$^{12}C(^{19}F,^{3}He)^{28}Al$	0.43	-

With formula 2.8 and 2.11 the following kinematics can be calculated:

Angle [^{o}]	Process	ion	Energy [MeV]	Pass 16μm Si
42	scattering	^{19}F	-	-
42	recoils	^{12}C	26	Yes

50 MeV $^{19}F \rightarrow {}^{9}Be$

With formula 2.8 and 2.11 the following kinematics can be calculated for 50 MeV $^{19}F \rightarrow {}^{9}Be$:

Angle [^{o}]	Process	ion	Energy [MeV]	Pass 16μm Si
42	scattering	^{19}F	-	-
42	recoils	^{9}Be	24	Yes

No data for the reactions are available.

50 MeV $^{19}F \rightarrow {}^{16}O$

The 50 MeV ^{19}F on ^{16}O process gives the following reactions, assuming a Coulomb barrier of 35.0 MeV. The data is taken from [WAY66] and formulas 2.13 and 2.12 are used.

Reaction	Q-value	Treshold [MeV]
$^{16}O(^{19}F,^{1}H)^{34}S$	16.4	-
$^{16}O(^{19}F,^{4}He)^{31}P$	15.8	-
$^{16}O(^{19}F,n)^{34}Cl$	10.5	-
$^{16}O(^{19}F,^{2}H)^{33}S$	7.2	-
$^{16}O(^{19}F,^{3}H)^{32}S$	4.8	-
$^{16}O(^{19}F,^{12}C)^{23}Na$	3.3	-
$^{16}O(^{19}F,^{3}He)^{32}P$	3.1	-
$^{16}O(^{19}F,^{6}Li)^{29}Si$	1.6	-
$^{16}O(^{19}F,^{7}Li)^{28}Si$	0.36	-
$^{16}O(^{19}F,^{10}B)^{25}Mg$	-5.1	11.2
$^{16}O(^{19}F,^{7}Be)^{28}Al$	-5.1	11.2
$^{16}O(^{19}F,^{9}Be)^{26}Al$	-5.4	11.8
$^{16}O(^{19}F,^{6}He)^{29}P$	-6.9	15.1

With formula 2.8 and 2.11 the following kinematics can be calculated:

Angle [^{o}]	Process	ion	Energy [MeV]	Pass 16μm Si
42	scattering	^{19}F	27.5	Yes
42	recoils	^{16}O	34	Yes
42	recoils	^{16}O	6.3	No

Appendix D

Pump down procedure

This pumping down procedure is for the detector test chamber at the -25^o beamline of the tandem lab.

PUMPING DOWN

- Close the air inlet
- Fill the cold trap of the rough pump with LN2
- Switch the rough pump on
- Open the rough pump valve
- Wait untill the pressure is 5 x 10^{-2} mbar
- Close the rough pump valve
- Switch off the rough pump
- Close the cryo pump valve
- Open the chamber valve
- Wait untill the pressure is 5 x 10^{-5} mbar
- Open the cryo pump valve

AIR INLET

- Switch off the bias voltages
- Close the chamber valve
- Open the air inlet
- Wait until the pressure is 1 bar

Appendix E

Minimizing procedure in Pascal

The next listing gives a enhanced version of the NAG FORTRAN E04CFF procedure.

```
{
This procedure minimizes (or fitting) function. The procedure is inspired
on routine E04CCF of the FORTRAN NAG library. Read the the NAG manual for
understanding of this concept. This procedure is described as 'robust but
slow'. The disadvantage of the procedure is that the parameters 'have to be
of the same order'. Therefore, I have changed the procedure in such a way
that the parameters are scaled. This removes the requirement for the
parameters.

A typical way to use the procedure is:

begin
    {Declare the start parameters}
  pm[0]:=-1e-2;
  pm[1]:=1.2;
  pm[2]:=3.8e2;
    {Stop criterium for the 'error' in the fit}
  err:=1e-8;
    {Maximum number of steps}
  steps:=25000;
    {Fit with 3 parameters}
  fite04j(3,pm,steps,err);
  writeln('a,b,c: ',pm[0],' ',pm[1],' ',pm[2]);
  writeln('Performed iterations: ',steps);
  writeln('Error in fit: ',error);
end.

In the main program, one has to declare the type:

type
  arretje=array[0..9] of double;

And the function that has to be minimized. The parameter i gives the number
of parameters in the array vl.

function fun(i:integer32;vl:arretje):double;
```

```
Remember that fitting a function with data points is just taking the
2-norm of the function with the datapoints.

E.J. van Veldhuizen 1994/1995
}

procedure fite04j(nop:integer32;var values:arretje;
                  var steps:integer32;var error:double);

var
  bf1,bf2:array[0..20,0..9] of double;
  res,finp,sca:arretje;
  vls:array[0..20] of double;
  deelf,rec,td,epsilon,upl,df:double;
  st,dp,x,y,new0,old0,nul0:integer32;

begin
  st:=0;
  dp:=0;
  df:=exp(ln(2)/nop);
  deelf:=1.9;
  epsilon:=1e-10;
  upl:=1e-10;
  for x:=0 to nop-1 do res[x]:=values[x];
    {Start first loop. This outer loop decreases the 'step size' with a
     factor 'df', until the step size < error or maximum number of
     iterations is exceeded }
  repeat
      {First, the scaling factors are determined out of the (numerical) 1e
       derivative of the function}
    dp:=dp+1;
    deelf:=deelf/df;
      {Set the coordinates for calculating the 1e derivative and put them
       in bf1 }
    for y:=0 to 2*nop do
    begin
      for x:=0 to nop-1 do
      begin
        bf1[y,x]:=res[x];
        if ((y+1) div 2 = (x+1)) and (y>0) then
        begin
          if y mod 2 = 1 then
          begin
            bf1[y,x]:=bf1[y,x]+epsilon;
          end else
          begin
            bf1[y,x]:=bf1[y,x]-epsilon;
          end;
        end;
      end;
    end;
      {Now the coordinates are set, calculate the scaling values and put
       them in sca }
    for y:=0 to nop-1 do
```

```
begin
  for x:=0 to nop-1 do finp[x]:=bf1[2*y+1,x];
  td:=fun(nop,finp);
  for x:=0 to nop-1 do finp[x]:=bf1[2*y+2,x];
  td:=0.5*(td-fun(nop,finp));
    {Limit the scaling factor to 1/upl }
  if abs(td)<upl*epsilon then
  begin
    if td<0 then td:=-1/upl else td:=1/upl;
  end else
  begin
    td:=epsilon/td;
  end;
  sca[y]:=td;
end;
  {Since the scalings factors are determined, one can start to
   calculate the values of the function around the start coordinate
   in the parameter space. }
for y:=0 to 2*nop do
begin
   {First calculate the coordinates, and put them in bf1}
  for x:=0 to nop-1 do
  begin
    bf1[y,x]:=res[x];
    if ((y+1) div 2 = (x+1)) and (y>0) then
    begin
      if y mod 2 = 1 then
      begin
        bf1[y,x]:=bf1[y,x]+(deelf*sca[(y-1) div 2]);
      end else
      begin
        bf1[y,x]:=bf1[y,x]-(deelf*sca[(y-1) div 2]);
      end;
    end;
  end;
end;
old0:=0;
repeat
  st:=st+1;
    {The next lines of code can be used to output some values (you
     interessed in) during the minimization. The 'if' statement
     controls that only after each (in this case) 50 iterations an output
     is printed}
  if st - (st div 50)*50 =0 then
  begin
    writeln(st,' ',dp,' ',rec);
  end;
    {Now the coordinates are set in bf1, calculate the function result
     and store it in vls}
  for y:=0 to 2*nop do
  begin
    for x:=0 to nop-1 do finp[x]:=bf1[y,x];
    vls[y]:=fun(nop,finp);
  end;
```

```
        {Search for the minimum value that was obtained, and store the array
         index of that value in new0}
      rec:=1e+30;
      new0:=old0;
      for x:=0 to 2*nop do if vls[x]<rec then
      begin
        rec:=vls[x];
        new0:=x;
      end;
        {Mirror all points in the point that had the minimum and store it
         in bf1}
      bf2:=bf1;
      for y:=0 to 2*nop do
      begin
        for x:=0 to nop-1 do
        begin
          bf1[y,x]:=2*bf2[new0,x]-bf2[y,x];
        end;
      end;
      if old0=new0 then nul0:=1 else nul0:=0;
      old0:=new0;
        {Stop if the same coordinate had the minimum value or when the
         stop criterium is reached}
    until (nul0=1) or (new0=0) or (deelf<err) or (st>steps);
    for x:=0 to nop-1 do res[x]:=bf1[new0,x];
      {The minimalisation is finished if the stop criteria are reached.
       Otherwise the loop is started again with a decreased step size}
  until (st>steps) or (deelf<err);
  for x:=0 to nop-1 do values[x]:=res[x];
  error:=rec;
  steps:=st;
end;
```

Appendix F

Stopping in silicon detectors

Next tables give an impression of the minimum energy required for an ion to pass a silicon detector. The values wre taken from [ZIEGL] for different ion up till ^{20}Ne.

ion	E [MeV] 10 μm	E [MeV] 30 μm	E [MeV] 140 μm	E [MeV] 300 μm	E [MeV] 1000 μm
^{1}H	0.73	1.5	3.6	6	13
^{4}He	2.6	5.7	13	24	50
^{6}Li	4.3	11	22	50	100
^{8}Be	6.8	17	34	75	150
^{10}B	9.0	22	46	105	210
^{12}C	11	28	60	135	260
^{14}N	13	35	75	165	340
^{16}O	16	43	92	205	420
^{19}F	19	50	115	225	510
^{20}Ne	20	58	130	260	600

ion	E/A [MeV] 10 μm	E/A [MeV] 30 μm	E/A [MeV] 140 μm	E/A [MeV] 300 μm	E/A [MeV] 1000 μm
^{1}H	0.73	1.5	3.6	6.0	13
^{4}He	0.65	1.4	3.3	6.0	15
^{6}Li	0.72	1.8	3.7	8.3	17
^{8}Be	0.85	2.1	4.3	9.4	19
^{10}B	0.90	2.2	4.6	11	21
^{12}C	0.92	2.3	5	11	22
^{14}N	0.93	2.5	5.4	12	24
^{16}O	1.0	2.7	5.8	13	26
^{19}F	1.0	2.6	6.1	12	27
^{20}Ne	1.0	2.9	6.5	13	30

Appendix G

The coupling of crystals

V. Avdeichikov from Dubna, Russia, has measured the effect of the different coupling between the crystal and (in his case) a photo multiplier tube. But the results can also be used for the coupling of a crystal with a photo diode. He used 1.173 MeV gammas emitted from a ^{60}Co source. The result is given as the amplitude of the signal in channels of the multi channel analyzer.

Coupling	Area	Amplitude for GSO	Amplitude for BGO
'Viscosil' oil	10 x 10 mm	1040	760
Dense contact	10 x 10 mm	650	490
0.15 mm airgap	9 x 9 mm	500	365

Appendix H

Time of Flight - Energy telescope

The next two pictures show components for the Time of Flight - Energy detector that will be built. Figure H.1 shows the time detector which is designed by H.J. Whitlow and is inspired on the Busch mirror detector. The applied voltages are given in the graph. These voltages can be made by a potential divider with a total resistance of 300 MΩ. Figure H.2 shows the total view of the design that I have made for mounting the time detectors and PiN-diodes.

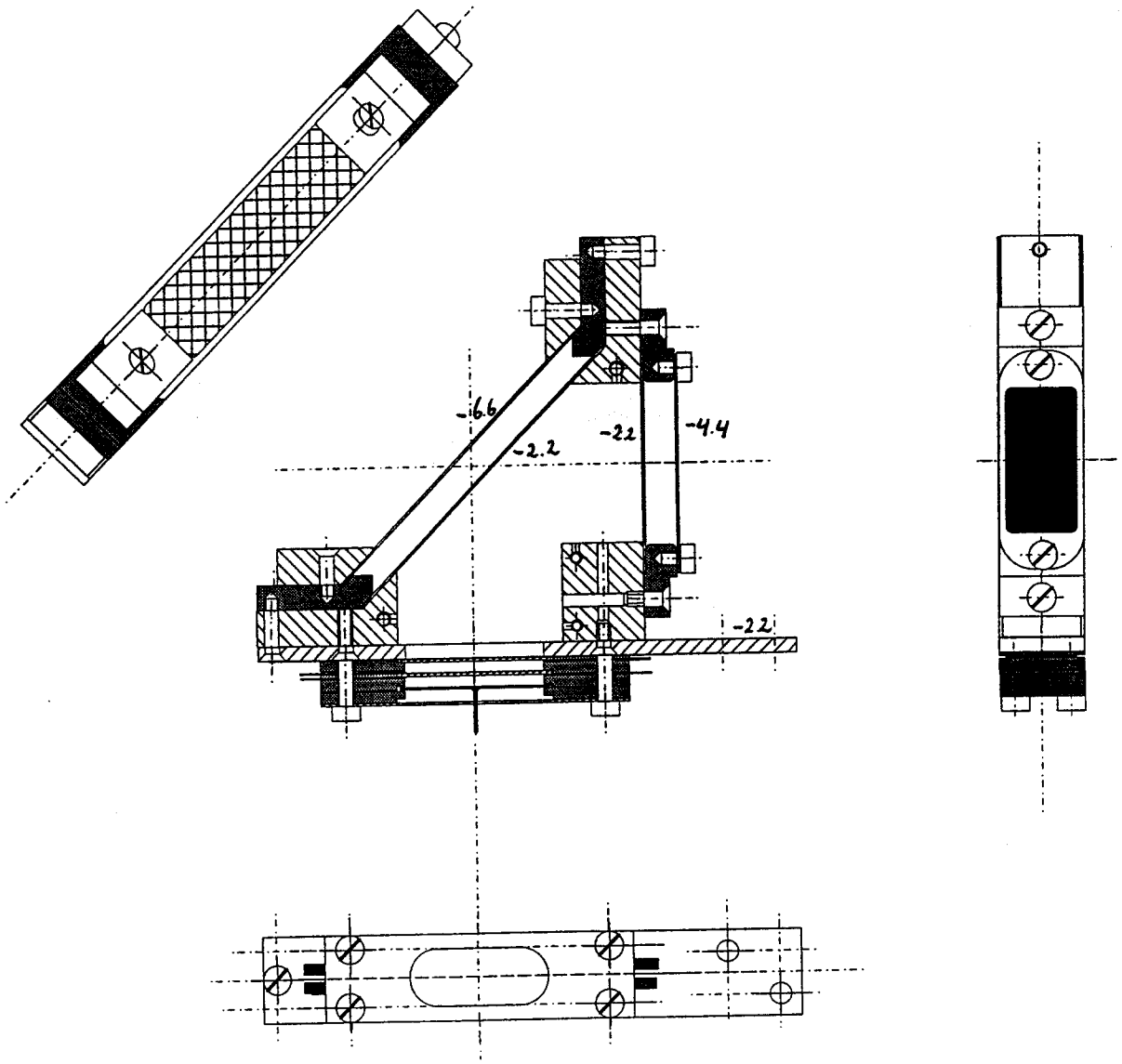

Figure H.1: *Drawing of the design of H.J. Witlow for the time detector that will be used in the CHICSi-telescope. The voltages are given in kV.*

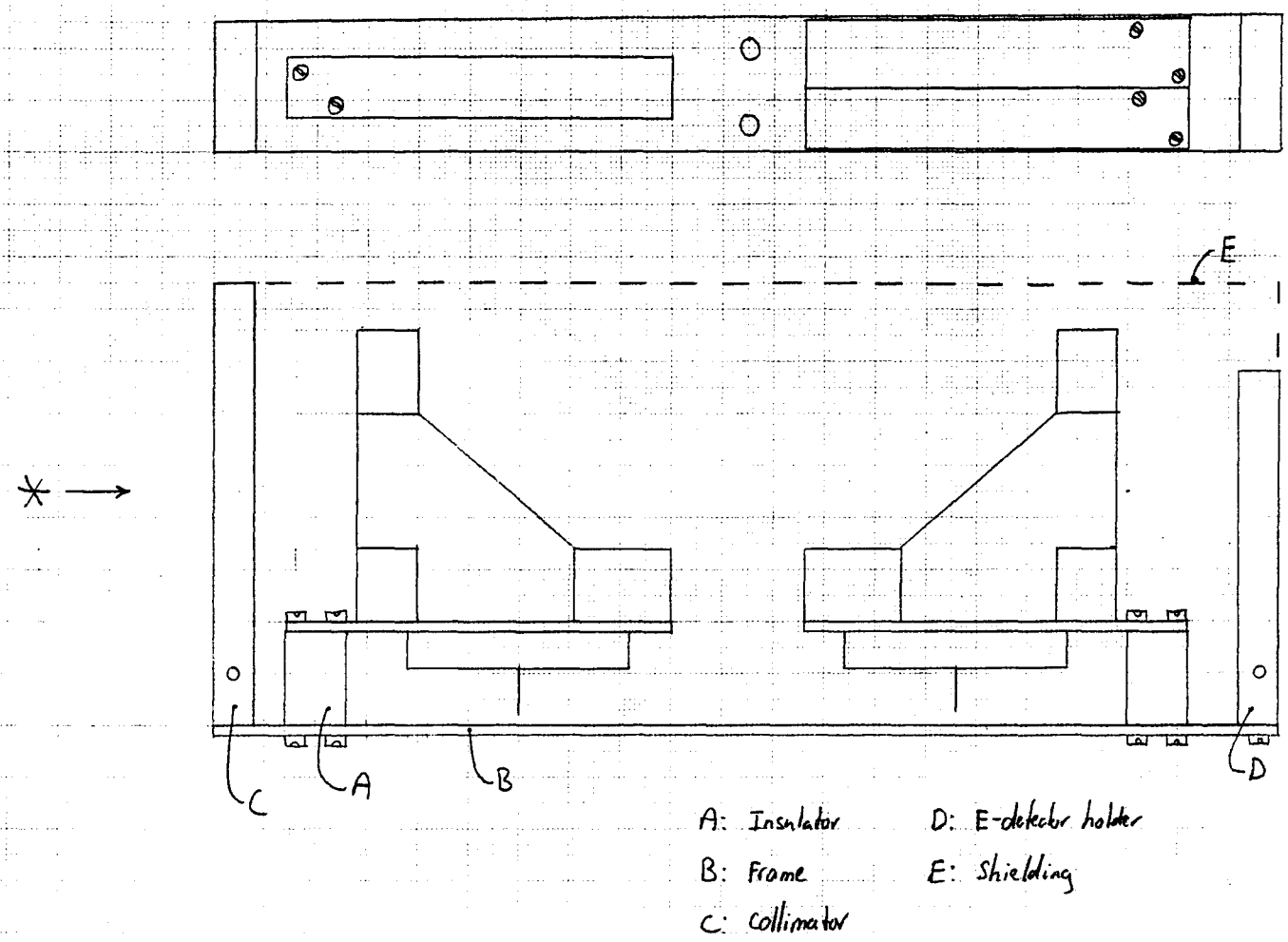

Figure H.2: *Drawing of the design for the Time of Flight-Energy telescope, for tests at the tandem detector test chamber.*

Appendix I

Monte Carlo simulation

Ions can leave a scintillation crystal at the side, without transferring all the energy to the crystal. The next graph gives the result of the Monte Carlo simulation done by V. Avdeichokov from Dubna, Russia.

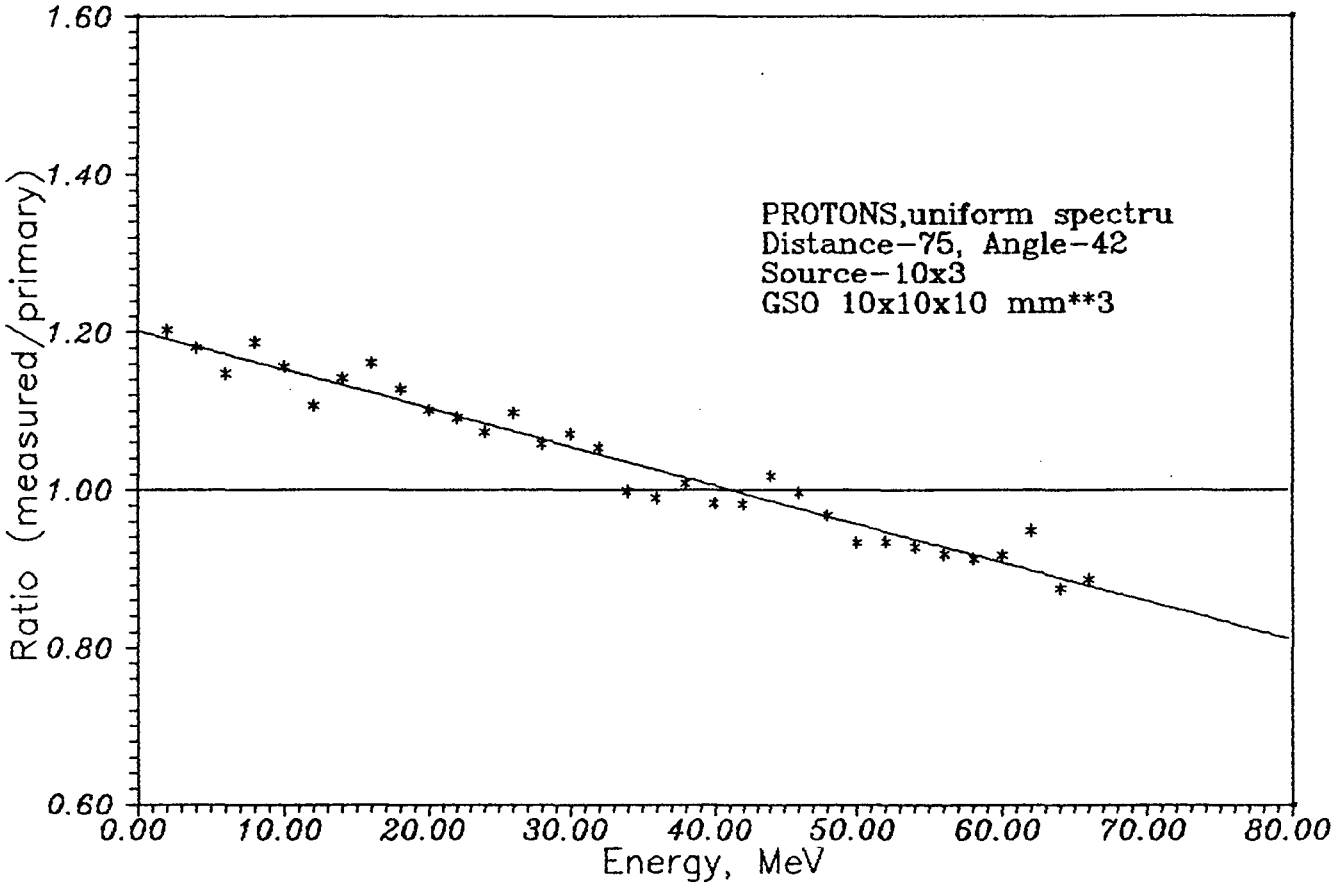

Figure I.1: *Monte carlo simulation with 5000 particles from a target on 5 cm distance and a GSO crystal with dimensions 10 x 10 x 10 mm.*

Appendix J

SLAC files

To perform simulations of electron trajectories, I have used the FORTRAN SLAC routines. I have converted the original program to APX VMS. Also I have written some utilities. They will be discussed below.

SLACA2.FOR

The file `SLACA2.FOR` is the FORTRAN source for the complete program. The (original) help text is given in the the beginning of the source. The program needs a file `for010.dat` as input file. This file contains the boundary and all other parameters that the program needs. During the run, the program produces a file called `SLACSPY.LIS` that tells which state the program has reached. The program produces two output files: `FOR008.DAT` and `FOR009.DAT`. The file `FOR009.DAT` contains all information about the boundary, electric fields and electron trajectories. The file `FOR008.DAT` contains information about the electron trajectories. This file can directly be used to make time histograms. For every electron, the file contains one line. The format of this line is: [electron number], [turn], [axial end coordinate] and [drift time]. The *turn* parameter can be 0 or 1. When it is 1, the electron has turned in axial direction. This is an indication that electrons oscillate inside the detector. The *axial end coordinate* gives the endpoint of the electron in mesh units. The *drift time* is given in pico seconds.

STPET02.DAT

The file `STPET02.DAT` contains the right boundary and parameters for the St. Petersburg detectors. It is a good idea to start with this file and to modify it for new problems. This file has to be renamed to `FOR010.DAT`, before starting the SLAC program.

PLT.FOR

The program `SLACA2` also produces a file `C.PLO`. This file contains a plot of the boundary, electric field lines and the electron trajectories. I have written `PLT.FOR`. This file converts the plot file to an Encapsulated Postscript (EPS) file. This EPS-files can be imported in most text processors.

MAKERAYS.C

To generate 1000 random secondary electrons with the distribution described in chapter 7, the program `MAKERAYS.C` can be used. It produces a file `RAYS.DAT` and `RAYS.GNU`. The first file is a text file that can be read in the `FOR010.DAT` file with a text editor. The file `RAYS.GNU` can be used for a graph program to display the electron-velocity distribution.